Simulation Study on the Transport of Biomedical Pickering Emulsion in Skeletal Muscle Tissue By Dissipative Particle Dynamics Method

A DISSERTATION

SUBMITTED TO THE DEPARTMENT OF

SCIENCE AND ENGINEERING OF

GUNMA UNIVERSITY FOR THE

DEGREE OF ENGINEERING

LIU XUWEI

GUNMA UNIVERSITY

DECEMBER 2023

Abstract

Lymph node targeting is a commonly used strategy in particulate vaccines, especially for Pickering emulsion. Extensive research for internal delivery mechanisms about Pickering emulsions, especially complex intercellular interactions of deformable Pickering emulsions, has been notably sparse, yet holds significant potential for enhancing vaccine efficacy.

This research provides an in-depth analysis of Pickering emulsions utilized as vaccine adjuvants, focusing on their transport mechanisms within the body at the tissue level. The innovative approach taken in developing a deformable albumin-stabilized Pickering emulsion caters to both intracellular and intercellular lymph node (LN) transfer pathways. This dual-pathway strategy significantly boosts antigen delivery, enhancing LN activation and stimulating a strong cellular immune response. Despite their promise, the complexities of Pickering emulsion transport, particularly the nuanced intercellular interactions, have been minimally addressed in scientific literature.

The study employs computational simulations to dissect the transport process into distinct sequential phases: muscular injection, passage through skeletal muscle tissue, lymphatic capillary navigation, and eventual LN accumulation. The role of antigen-presenting cells like dendritic cells is emphasized, alongside the mechanical behavior of lymphatic endothelial cell flaps which facilitates the transport of flexible particles. A sophisticated mesoscale model based on the dissipative particle dynamics (DPD) simulation method is enhanced, leading to a deeper understanding of scaling factors and cellular diversity in drug delivery systems.

The integration of the DistMesh algorithm represents an innovative step in depicting the cytoskeleton of various cell shapes, confirmed by the mechanical response of red blood cells during stretching tests. This aligns well with experimental findings and supports further investigation into cellular mechanics.

Additionally, the study meticulously investigates the factors influencing the transport efficiency of Pickering emulsions in skeletal muscle tissue. It finds that variables such as the conservative force parameter in the DPD method, local tissue environmental conditions, viscosity, temperature, and initial velocity all contribute to transport efficiency, with the orientation of initial velocity vectors towards the axial direction of cells being particularly beneficial.

This work not only sheds light on the behavior of flexible droplets in cellular environments but also paves the way for future exploration into cellular mechanical properties and the organization of biological activities at the cellular level. The insights gained are pivotal for the ongoing development and optimization of biomedical materials, particularly for vaccine delivery.

Keywords:

Pickering Emulsion, Muscular Cells, Transport Phenomena, Dissipative Particle Dynamics, Lymphatic Capillaries, Drug Delivery, Targeting Lymph Node

Contents

Chapter 1 Introduction

1.1 Background

1.1.1 Vaccine targeting lymph node

At the beginning of 2020, the COVID-19 virus swept across the world, bringing significant losses to people [1,2]. Researchers promptly commenced studies on vaccine development and preparation. Traditional vaccines generally use attenuated or inactivated viruses. After being introduced into the human body, these vaccines elicit an immune response. However, these methods have risks, including incomplete inactivation or even restoration of viral virulence. With technological development and scientific progress, substantial achievements have been made in the research of recombinant protein vaccines, split vaccines, peptide vaccines, and so on.

There are some reasons that vaccines target lymph nodes: Firstly, lymph nodes are immunological hubs, which are central to initiating adaptive immune responses, where lymphocytes such as T and B cells become activated; Secondly, professional antigen-presenting cells (APCs) within lymph nodes productively capture and expose vaccine antigen to lymphocytes to achieve effective antigen presentation; Thirdly, targeting lymph nodes helps in the generation of long-lived memory cells, key to sustained immunity due to the mechanism of memory cell induction; Fourth, concentrating vaccines in lymph nodes can intensify the immune system's recognition and response to the vaccine components. Thus, targeting lymph nodes aims to enhance vaccine efficacy by harnessing the immunological functions concentrated within them. Consequently, vaccines targeting the LNs hold significant promise for immediate engagement with antigen-presenting cells (APCs), which induces strong antibody production, T-cell activation, and anti-cancer outcomes. [3–5]

To facilitate drug delivery to the lymph nodes, there are various inoculation methods available: First, subcutaneous and intradermal injections can directly target the lymphatic system, suitable for macromolecules and nano-preparations, however, it may require more expertise to inject accurately and may cause discomfort at the injection site; Secondly, the intravenous injection can rapidly enter the blood circulation and is very effective for drugs requiring systemic action, however, the direct targeting ability to lymph nodes is weak, and the drug may be absorbed or degraded by other parts of the body before reaching the target; Thirdly, intra-lymph node injection which is directly acting on lymph nodes, can reduce systemic exposure to drugs and increase local concentration, however, the operation is technically demanding, may increase the risk of infection, and may be more painful for the patient. [6]

1.1.2 Emulsion

In an oil-water mixed system, due to the immiscibility of oil and water, the Gibbs energy of the formed dispersion system is high, rendering the system unstable. To obtain a stable system, emulsifiers, typically surfactants, are often added to the oil-water mixture. The surfactant's tail chain penetrates the oil, with the head group anchoring at the oil-water boundary, providing stability to the system referred to as an emulsion. There are two primary emulsion categories: oil-in-water (O/W), where oil droplets are scattered within a water matrix, and water-in-oil (W/O), where water droplets are embedded in an oil environment. In O/W emulsions, oil forms the dispersed phase against a water backdrop, the continuous phase. Conversely, W/O emulsions have water droplets interspersed within a continuous oil medium. Both emulsion types consist of one phase dispersed as droplets within another, termed emulsion droplets. [7,8]

Emulsions have numerous diverse applications. For example, in oil extraction, microemulsions with particle sizes below 100 nm are commonly used as oil and gas

production aids for chemical flooding and fracturing fluid displacement. In the petrochemical industry, it is difficult to separate mixtures of hydrocarbons with similar boiling points using conventional methods. However, by placing the mixture in a surfactant-containing aqueous solution, a stable O/W emulsion forms, encapsulating the components to be separated and rising into the organic solvent. Through selective permeation, separation can be achieved. Additionally, in wastewater treatment, the liquid film of emulsions is often used for extracting metal ions from mixtures, a method far more efficient than traditional extraction techniques. This liquid membrane technology allows for the effective separation of impurities, thereby purifying water. In the daily chemical industry, common products like creams, hair milk, gels, and conditioners fall under the category of emulsions. In the biopharmaceutical industry, Dieng and others have researched the use of particle-stabilized nanoemulsions for drug delivery. Results show that particle-stabilized emulsions can significantly improve drug resistance to stomach pH and achieve controlled drug release. This technology applies to the oral administration of insoluble drugs. Furthermore, emulsions are also applied in vaccines, which will be elaborated on in the following discussion regarding their use as adjuvants in vaccines.[9]

1.1.2.1 Pickering emulsion

Pickering emulsions, a century-old discovery, have witnessed a resurgence in interest in recent decades. Their unique stabilization mechanism, facilitated through the action of solid particulates at the junction between oil and water, sets them apart from traditional emulsions. By leveraging solid particles as stabilizers instead of conventional surfactants, Pickering emulsions exhibit enhanced stability against coalescence and present a myriad of advantageous properties. When designed with biocompatible solid particles, these emulsions become particularly promising for *in vivo* applications, leading to widespread adoption in diverse sectors ranging from biomedicine to cosmetics [10].

In the comparative analysis of Pickering emulsions and traditional surfactant-stabilized emulsions, several key advantages of Pickering emulsions have been identified [10–12]: Stability: Research indicates that Pickering emulsions demonstrate superior resistance to droplet flocculation and coalescence, thereby ensuring enhanced long-term stability. Biocompatibility: Studies suggest that when employing solid particles deemed safe for in vivo use, Pickering emulsions exhibit increased biocompatibility, a factor critical for applications in drug delivery and biomedical fields, which in turn reduces the potential for adverse effects and toxicity. Environmental Impact: Literature supports the notion that Pickering emulsions, due to their reduced reliance on chemical surfactants, are more environmentally benign compared to their traditional counterparts. Economic Viability: Analyses reveal that the production of Pickering emulsions can be more cost-effective, primarily attributed to lower production costs and minimized dependency on chemical surfactants. Customizability: Empirical evidence suggests that the selection of diverse solid particles during the creation of Pickering emulsions allows for tailoring of their physical and chemical attributes, catering to specific requirements of varied applications. These findings elucidate the substantial potential of Pickering emulsions, particularly due to their unique stabilization mechanism and the ability to tailor their properties, rendering them highly suitable for applications necessitating heightened stability and biocompatibility.

Pickering emulsions have multifaceted applications in the biomedicine [13], attributed to their intrinsic high stability, low toxicity, and exceptional biocompatibility. Notably, PEs are being actively researched for their utility in antitumor treatments, providing a novel approach to oncological therapies. They are also explored as carriers for antiviral drugs, offering new strategies to combat viral infections. In the domain of biosensing, Pickering emulsions serve as platforms for enhanced signal detection and amplification, while their role in biocatalysts involves safeguarding enzymes for

improved biochemical reactions. Additionally, their contribution to wound healing signifies their potential in tissue repair and skin regeneration. The versatility of Pickering emulsions extends to various other applications, including skincare, where their protective qualities are harnessed for therapeutic benefits.

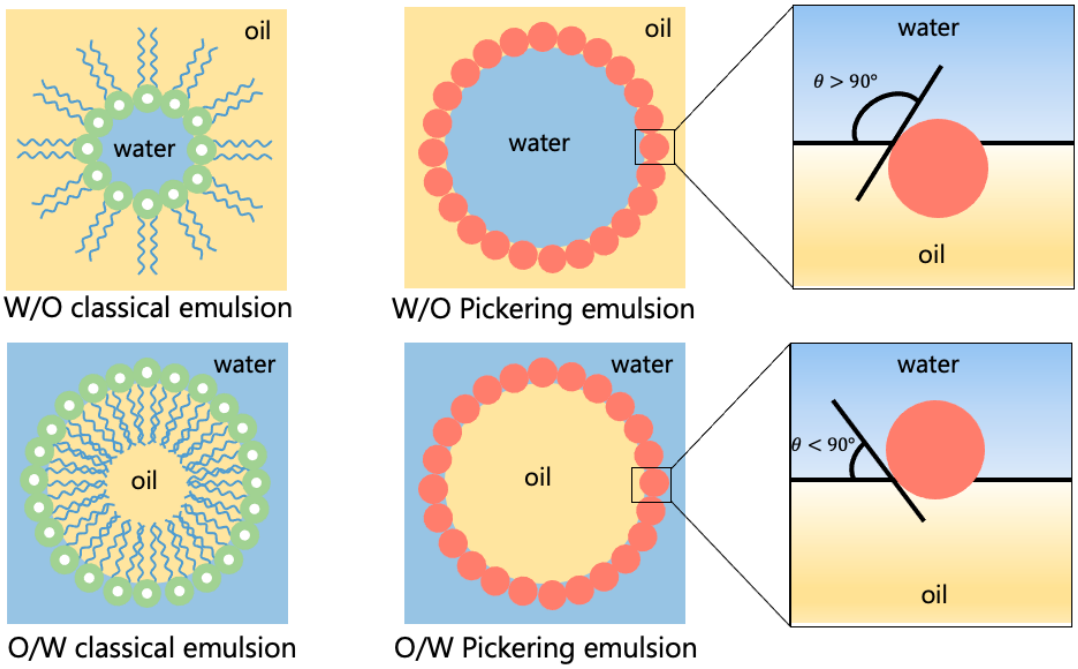

Figure 1 The Illustration of the Difference of Pickering Emulsion based on Particle and Classical Emulsion Based on Surfactants

1.1.3 Pickering emulsion for the enhanced drug delivery systems

Due to distinctive characteristics, Pickering emulsions have become notably prominent in drug delivery applications. The solid particles that stabilize Pickering emulsions provide a robust barrier to coalescence, resulting in enhanced stability. This is crucial for drug delivery systems, where stability of the carrier notably affects efficacy and release profile of the encapsulated drug. Solid particulates within Pickering emulsions may be tailored to regulate drug dispensing velocity. By manipulating the particle size, surface chemistry, and porosity, it is possible to achieve sustained, delayed, or targeted drug release. This is especially beneficial for drugs that require controlled release to maintain therapeutic concentrations over extended periods. Pickering

emulsions can be designed for targeted drug delivery. By modifying the surface properties of the stabilizing particles, it is possible to direct the emulsion to specific tissues or cells. This targeted approach can increase the therapeutic efficacy and reduce side effects. Xia and colleagues harnessed the immunogenic properties of Pickering emulsions for use as vaccine adjuvant and delivery strategy. This highlighted the distinct softness and flexibility of Pickering emulsion in cellular interactions, showing its vast promise for biomedical uses [14]. Xia's research group summarizes some recent progress of Pickering emulsions and their applications for drug delivery systems and proposes a more comprehensive understanding of the tuning aggregating particles and the underlying mechanism to improve the efficiency of drug delivery systems [15]. The aggregating particle properties dictating the formation of Pickering emulsion include the following factors: size, shape, wettability, and charge. Furthermore, this review discusses the structure-effect relationship, as well as aspects related to strategic loading, efficient delivery, and controlled release. Among them, to achieve efficient drug delivery, some different multi-scale barriers need to be tacked out from the tissue level which is a distribution of Pickering emulsion inside the organ or tissue or intercellular substance to the target tissue, the cellular level which is related to the cellular uptake process to obtain the high cellular concentrations, and the subcellular level which is related to the cytosolic delivery process to achieve the endosomal degradation of drugs.

Xia's team has crafted a flexible albumin-based Pickering emulsion. Upon injection into muscle tissue, this emulsion navigates through cellular junctions and endothelial spaces, enabling a direct conduit to lymph nodes via an intercellular route. Its substantial size also permits retention at the site of injection, optimizing antigen uptake and APC activation, alongside targeted lymph node vaccine delivery through an intracellular route. Unlike solid particles that solely trigger an immune response intracellularly, this dual lymph node targeting approach markedly increases antigen concentration and lymph node activation, thereby potentizing cellular immunity and

improving survival in mice with tumors. Their research, utilizing indicators to label antigens, the cytoskeleton, and lymphatic endothelial cells, demonstrates that particle-stabilized emulsions indeed accumulate within lymph nodes (LNs). Furthermore, by marking Resident Dendritic Cells (DCs) and Migratory DCs within LNs, the presence of an intercellular pathway for drug delivery is confirmed. However, the detailed mechanism of the intercellular pathway for drug delivery via Pickering emulsions requires further investigation.

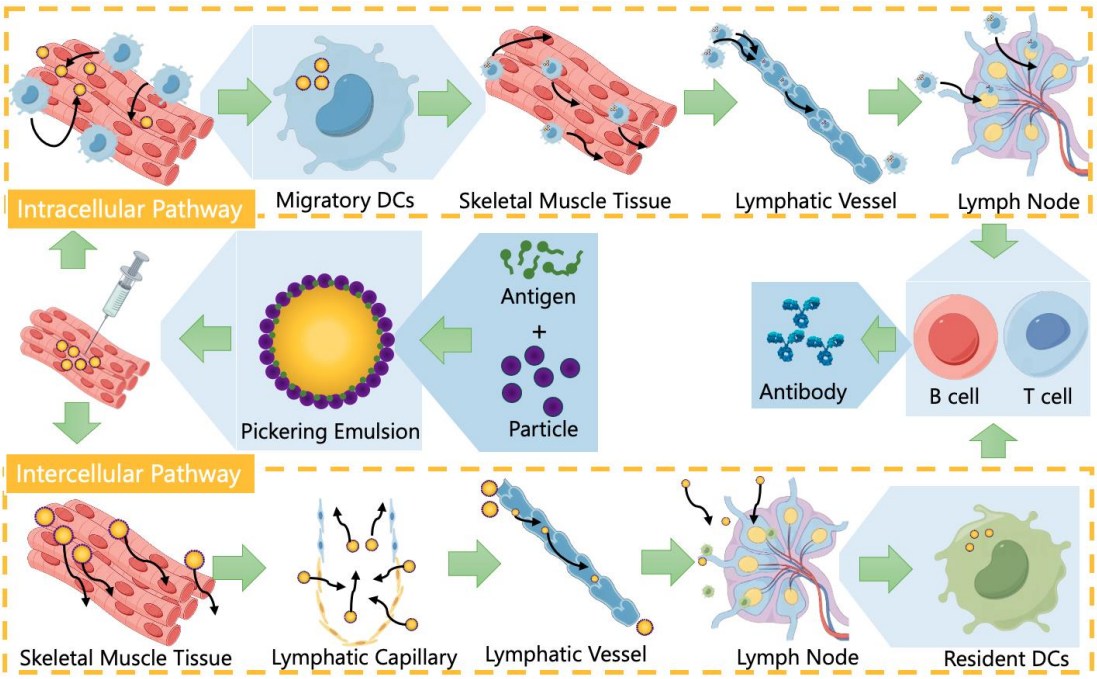

Figure 2 The scheme of Different Pathways of Drug Delivery Based on Pickering Emulsion from Tissue Level.

Figure 2 elucidates the delivery process of Pickering emulsion through intracellular and intercellular pathways at the tissue level. The fundamental difference between the two pathways lies in the site of binding between Pickering and immune cells specialized in antigen presentation, like dendritic cells, one kind of APCs. For the intracellular pathway, larger-sized particulate vaccines (greater than 200nm) typically remain close to the site of administration, where potent cytokines and chemokines, along with co-stimulatory molecules, draw in and stimulate APCs, including dendritic cells.

Subsequently, this stimulates the uptake of antigens by APCs, activation, and delivery to the lymph nodes, thereby enriching antigens within the lymph nodes. For the intercellular pathway, particles maliciously move through the interstitial flow within the body tissue, cross the intercellular gaps, and passively drain into the lymphatic vessels within the muscle tissue, accumulating in the lymph nodes and further activating APCs residing in the lymph nodes. APCs present antigens to the surrounding immune cells, including T cells and B cells, thus generating an adaptive immune response early in the vaccination process. The main difference between the two pathways is where the vaccine particles meet the meet immune cells that show antigens, like dendritic cells. In the intracellular pathway, big vaccine particles stay near where they are injected. Here, strong immune signals and other molecules attract and activate these immune cells. These cells then take up antigens and carry them to the lymph nodes, making the lymph nodes full of antigens. In the intercellular pathway, particles move through the spaces between cells, enter lymphatic vessels by themselves, and end up in the lymph nodes. There, they activate immune cells that live in the lymph nodes.

Through the analysis of histological cell morphology [14,16–24], the transport process of vaccines employing Pickering emulsion droplets involves a series of distinct stages for intercellular pathway. Initially, in Stage 1, the droplets are introduced into the body via intramuscular injection. Following this, in Stage 2, they navigate through the intercellular matrix space between skeletal muscle cells. Subsequently, in Stage 3, the droplets enter the lymphatic capillaries, facilitated by the gaps in lymphatic endothelial cells (LECs). This leads to Stage 4, where the droplets flow through lymphatic vessels to reach the lymph nodes. Finally, in Stage 5, the antigen contained within the Pickering emulsion droplets activates the immune response at the lymph nodes, culminating in the vaccine delivery process. We schematically illustrate the lymph node transfer process of soft droplets in the following Figure 3. This process is still complicated, and we can convert different stages into similar solved problems.

Stage 2 is like the particular colloid diffusion movement in confined spaces. Stage 3 is to try to figure out how changes in tissue pressure regulate the opening and closing of lymphatic capillary endothelial cell microvalves. Stage 4 is similar to blood flow in blood vessels. In summary, analyzing the drug delivery process from the perspective of cellular and tissue levels represents a mesoscale challenge. The SEM images show the physiological relationship and structure of related tissues and cells. The Figure 4 illustrates the relationship. LY stands for the lymphatic capillary, SKM stands for several muscle layers, and V stands for the venular microvessels.

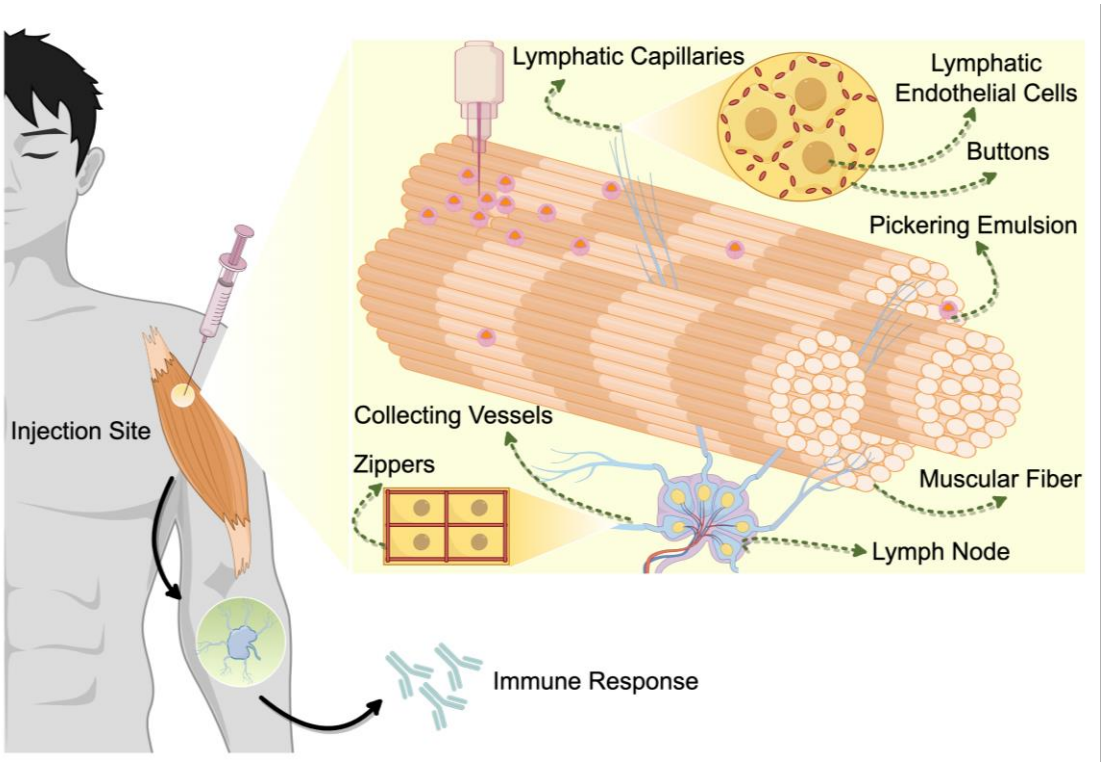

Figure 3 Schematic Illustration on the Lymph Node Transfer of Pickering Droplets

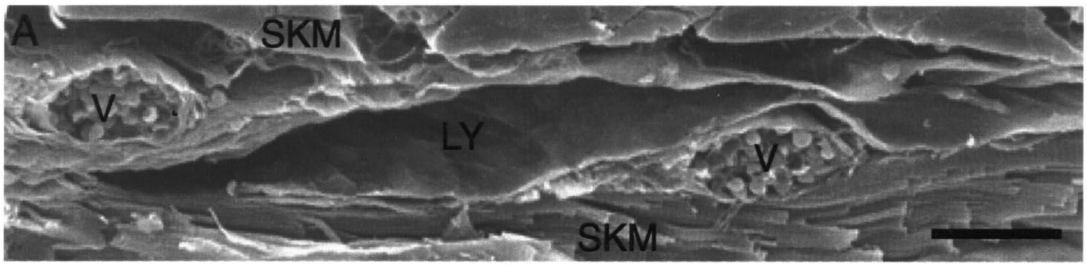

Figure 4 Scanning electron micrographs of lymphatic capillary as viewed in inclined sections through the muscle tissues [25]

1.2 Analysis of the scale of research problems from biology

Given that the research scope of this topic is centered on the cellular and tissue levels in biological organisms, it is imperative to systematically elucidate the relationships between the constituent units at different hierarchical levels. Furthermore, for the specific research subject, it is crucial to clearly outline the physiological characteristics of the relevant cells and tissues. Doing so will establish a defined physical context for constructing models and simplifying problems, thereby facilitating subsequent quantitative analysis.

1.2.1 Hierarchical levels of a biological system

An organism, as a whole, is characterized by its highly organized and structured hierarchy, which can be deconstructed either in a top-down direction from large too small or in a bottom-up direction from small-to-large as shown in Figure 5. From a bottom-up perspective, the hierarchical structure of an organism begins at the most fundamental level with atoms, such as hydrogen, oxygen, and carbon, which are the smallest units of matter. These atoms combine to form a wide array of biomolecules, which vary greatly in size and structure and perform diverse functions. The four major types of macromolecules include nucleic acids, proteins, carbohydrates, and lipids and smaller molecules include water, ions, metabolites, and hormones. At the subcellular

level, which is shown in Figure 6, molecules aggregate to form more complex structures like organelles and the cytoskeleton. Organelles (such as mitochondria, endoplasmic reticulum, and Golgi apparatus) perform specific biological functions, including energy transformation, protein synthesis, and secretion. The cytoskeleton provides structural support and shape to the cell and is involved in cell movement and division. From the perspective of cellular level, the smallest fundamental unit of structure and function in a living organism, various molecules and subcellular structures within the cell work together to enable the cell to perform a wide range of functions, including metabolism, proliferation, and response to external environmental changes. Tissues represent the next level in this hierarchy, linking cellular structure to organ systems. Tissues are groups of cells with common structures and functions and the four main tissue types in humans include muscular, epithelial, nervous, and connective. Further up the hierarchy, organs form from the assembly of different tissue types. Each organ, such as the brain in the nervous system or the stomach in the digestive system, performs specific functions and works collaboratively within organ systems. At the highest level of organization, the organism is a complex integration of various organ systems, including the respiratory, digestive, nervous, cardiovascular, and muscular systems. These systems work in unison to maintain the organism's overall function and homeostasis, highlighting the intricate and interconnected nature of biological structures from the smallest atomic level to the complete organism.[26,27]

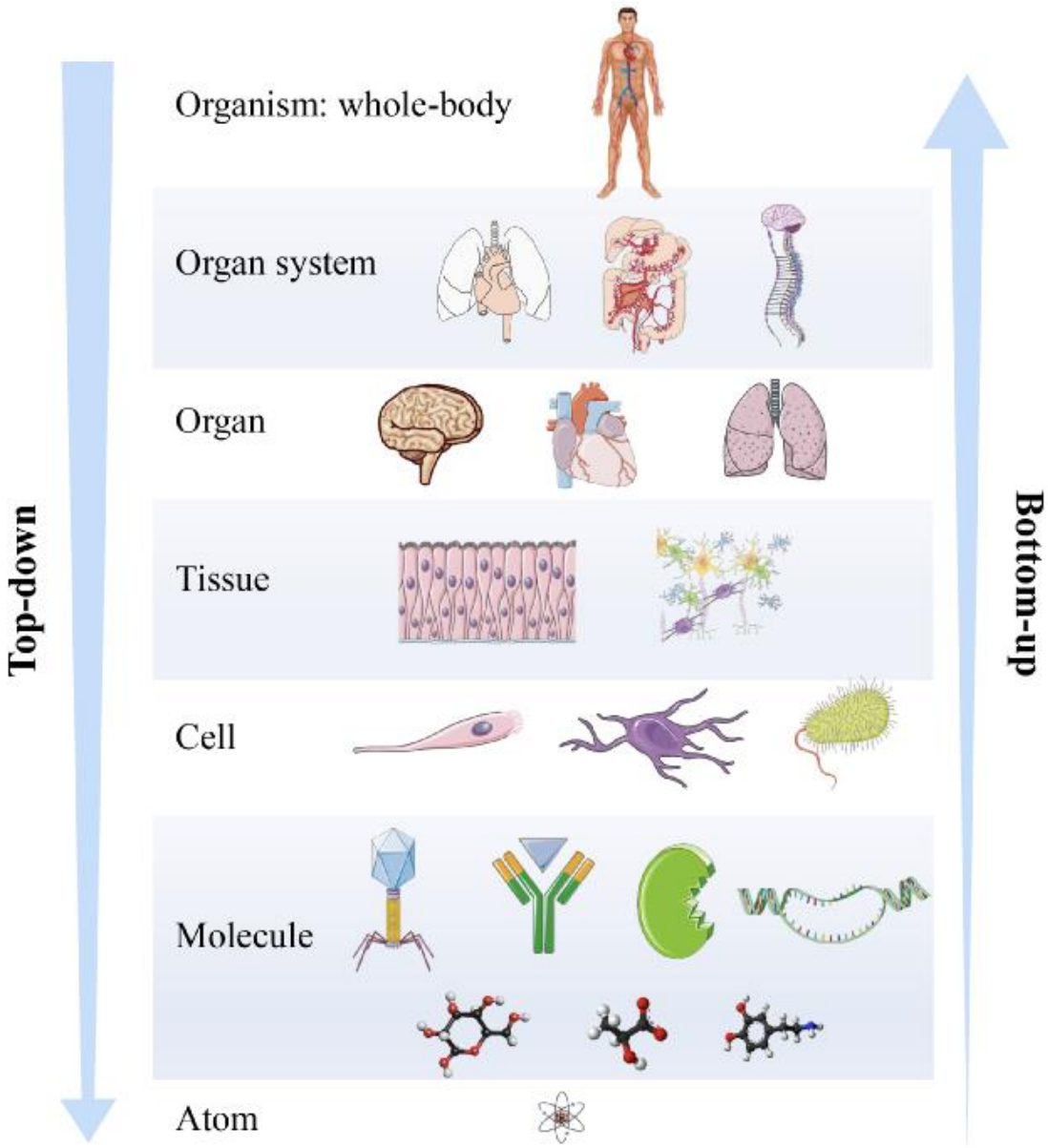

Figure 5 The illustration of the hierarchy structure for human [26]

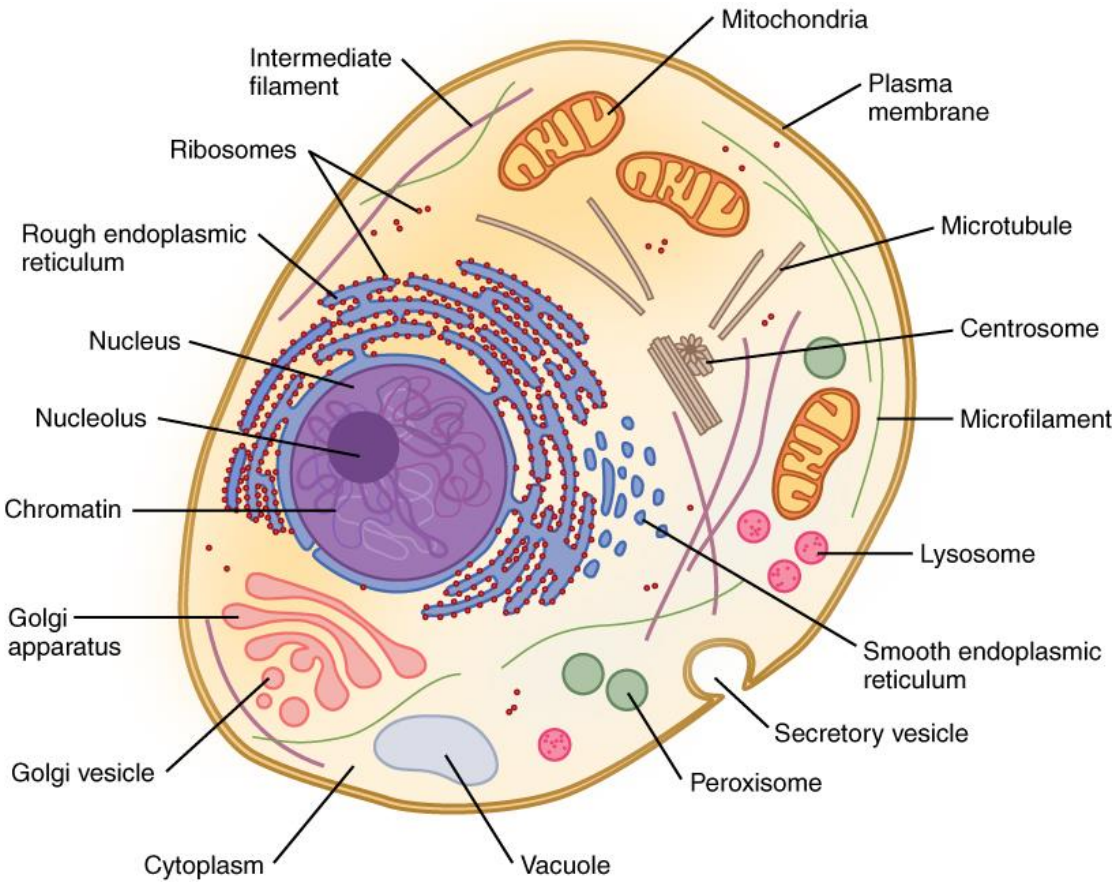

Figure 6 A generalized diagram of an animal cell [27]

1.2.2 Physiological characteristics of related tissues and cells

Given the objective of research to understand underlying mechanisms of drug delivery methods at the tissue level and considering the lack of previous systematic research in this area, it is essential to have a clear understanding and summary of the cellular morphology and mechanical properties of the basic units composing tissues. Therefore, this section provides a systematic overview of the primary tissues and morphologies involved in the drug delivery process, and through this review, clarifies the tissue environment related to the delivery pathway for Pickering emulsions. The procedure of intramuscular injection primarily engages the skeletal muscle and lymphatic structures belonging to the immune system, encompassing lymph capillaries, lymphatic vessels, and lymph nodes.

1.2.2.1 Skeletal muscular tissue

Muscle tissue contains a rich array of immune cells and capillaries, facilitating the absorption and distribution of vaccine components. When injected into muscle, these components enter the circulatory system more effectively, triggering an immune response. Additionally, the arm's proximity to axillary lymph nodes allows vaccine components to enter the lymphatic system and activate a systemic immune response through the activity of immune cells.

Muscle cells, also known as muscle fibers, are visible within muscle tissue and the illustration of muscular tissue is shown in Figure 7. These cells are elongated, tubular in shape, and develop from muscle stem cells (myoblasts). After muscle formation, muscle cells differentiate into various types, including skeletal, smooth, and cardiac muscles. Skeletal muscle is responsible for body movements; cardiac muscle primarily facilitates heartbeats and blood circulation. Smooth muscle is associated with blood vessel walls, the digestive tract, and the respiratory system. [18,21]

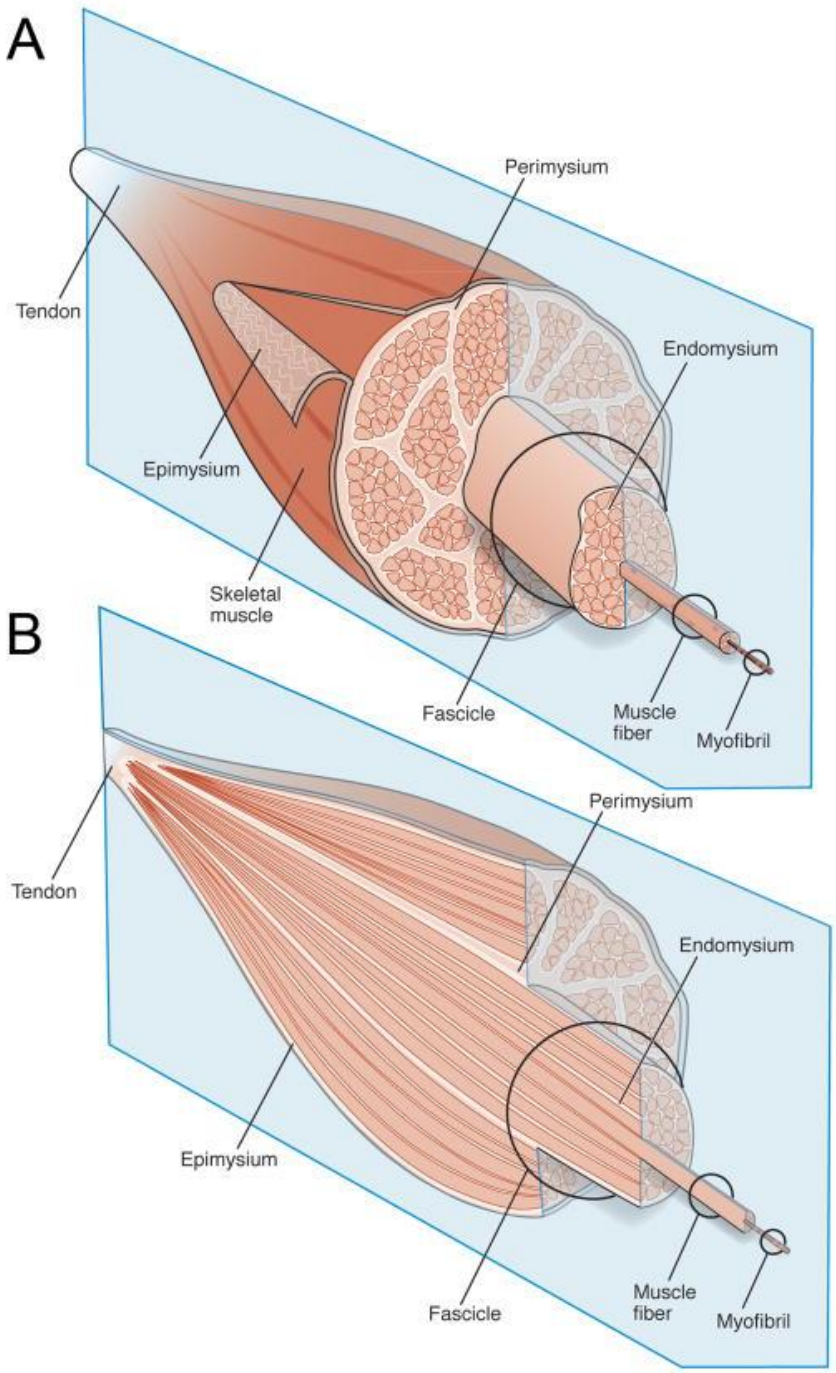

Figure 7 A diagram of the skeletal muscle tissues [28]

Muscle tissue (skeletal muscle) is organized from the macroscopic to the microscopic level as follows [18,28–30]:

Muscle: This is the most macroscopic level, where muscle comprises numerous muscle cells (or fibers). Muscles are responsible for body movement and posture maintenance. The length and diameter of muscles vary based on location and function

interior the body. For example, thigh muscles are larger in length and diameter than arm muscles.

Fascicle: A fascicle refers to a bundle of fibers or cells in biological tissues. This term is commonly used to describe the structure of muscle tissue.

Muscle Fiber: Muscle fibers are essentially muscle cells and form the basic unit of muscles. Each muscle fiber consists of many myofibrils. The length of muscle fibers typically ranges from a few millimeters to several centimeters (2-3 cm), with a diameter of about 10 to 100 micrometers.

Myofibril: Myofibrils are structures within muscle fibers, composed of numerous myofilaments. They are the fundamental units of muscle contraction. Myofibrils usually have the same length as muscle fibers, as they are components of the fibers. The diameter of myofibrils is about 1 micrometer.

Myofilament: Myofilaments are protein filaments that make up myofibrils. There are two primary types of myofilaments: actin (thin filaments) and myosin (thick filaments). Muscle contractions are produced by the sliding of these filaments. Myofilaments are about 1 to 2 micrometers in length, with a diameter of a few nanometers.

1.2.2.2 Immune system

The lymphatic network comprises vessels, nodes, and related organs. Interstitial fluid is absorbed by small capillary lymphatics [20], which coalesce into larger precollectors, collectors, trunks, and ducts, as depicted in Figure 7. This fluid, now termed lymph, is propelled through rhythmic contractions of vessel walls, equipped with smooth muscle, while one-way valves inhibit reverse flow. Lymph progresses from capillary lymphatics, through collectors, to lymph nodes.

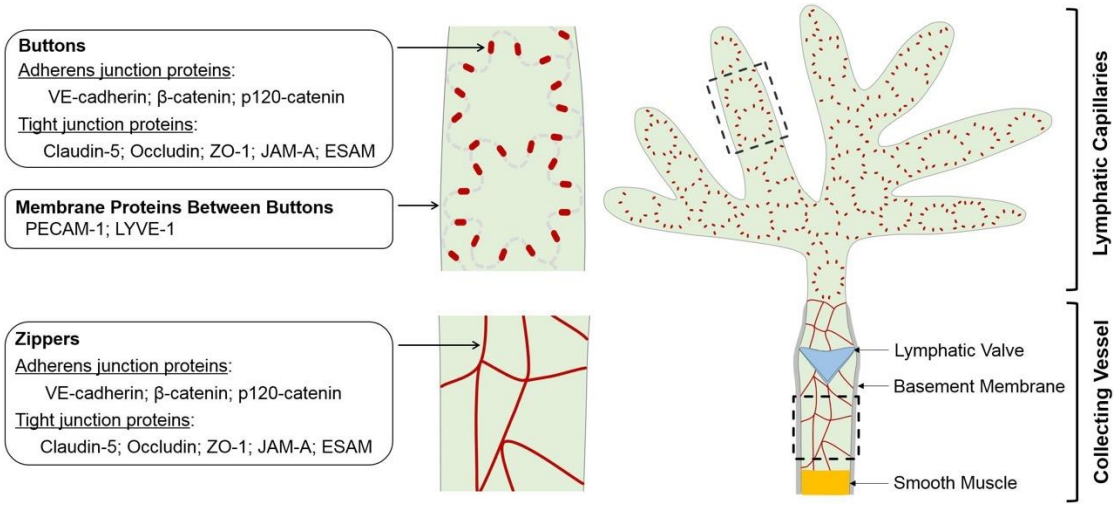

Figure 8 Illustration of structures of lymphatic capillaries and lymphatic vessels[24]

Capillary lymphatics have diameters ranging from 10 to 60 micrometers, with wall thicknesses between 50 to 100 nanometers, and terminate blindly. Openings in the capillary endothelium, functioning as one-way valves, permit lymph entry. These valves open when interstitial pressure rises, allowing fluid into the lymphatics, and close when internal pressure mounts.

Lymphatic Endothelial Cells (LECs) have special intercellular connections known as "buttons," including both adherent junctions and tight junctions [16]. Capillary lymphatic endothelial cells measure 49 micrometers in length and 18 micrometers in width. The diameter of anchoring filaments (buttons) is 6-10 nm, and they are 15-30 nm wide. Buttons are irregular junctions between the overlapping, finger-like protrusions of adjacent endothelial cells in initial lymphatics, laden with proteins from adherents and tight junctions, creating anchor points for neighboring LECs aligned with the cell margin. The flap tips between buttons have a loose overlap, facilitating free entry into the lymphatics, propelled by the pressure gradient from interstitial space to lumen. Figure 9 depicts the anatomy of lymphatic capillaries, with sections C-E showcasing the endothelial openings of these capillaries.

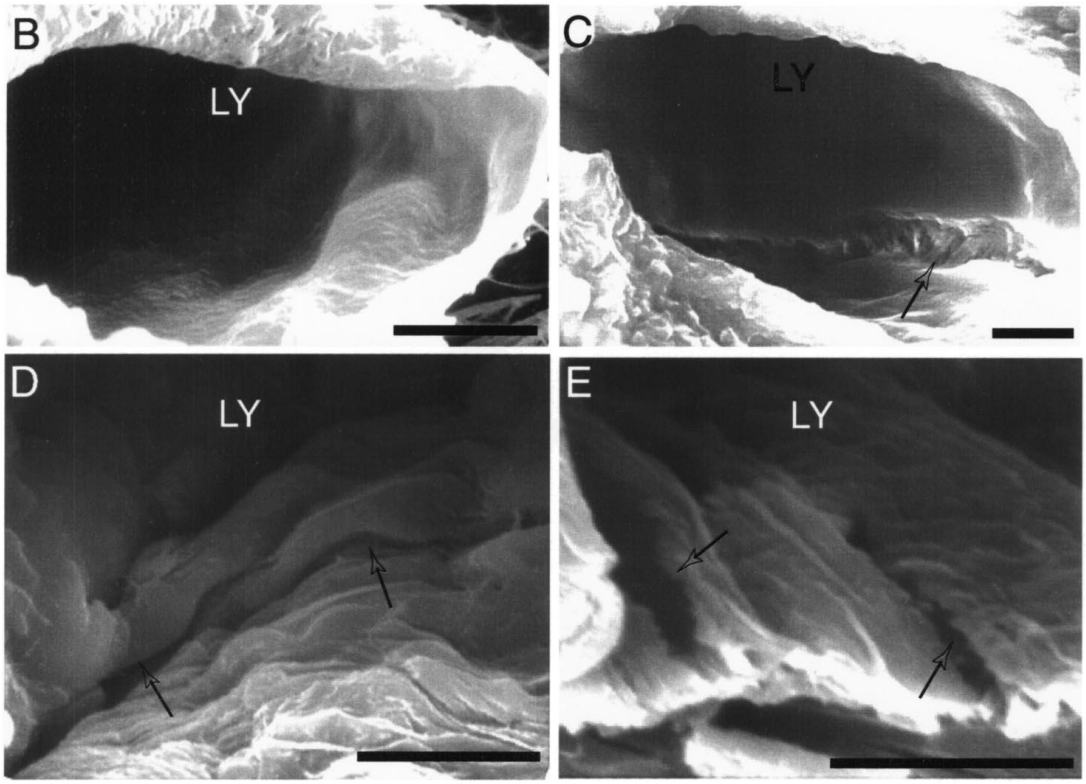

Figure 9 Scanning electron micrographs of the inner of the initial lymphatics[25]

Dendritic cells are regarded as the most effective professional antigen-presenting cells, pivotal in orchestrating immune defense against pathogens and maintaining self-tolerance and non-reactivity to benign environmental antigens [31]. DCs capture pathogens or their parts, process these antigens, and present them in a form that is recognizable to T-cells, initiating a specific immune response in the lymph node.

1.3 Innovation of research

1.3.1 Current research challenges

Comprehensive studies elucidating the intracorporeal delivery mechanisms of Pickering emulsions, especially the intricate intercellular interactions of deformable Pickering emulsions, remain significantly scarce and have historically received minimal attention. Yet, they play a crucial role in vaccine efficacy.

The current understanding of the drug delivery process, particularly quantitative analysis and simulated models is still quite limited. Most knowledge of this process, especially for soft and deformable droplets like Pickering emulsions, remains vague.

At present, the depth of understanding and simulation of internal kinematics at the tissue level within the human body is profoundly limited, and there is a significant lack of effective models.

1.3.2 Targets of research

Develop a model system suitable for representing the coexistence of Pickering emulsions and cells, which can adequately characterize their transport processes and kinetic behaviors; analyze the drug delivery process within skeletal muscle tissue, employing simulation methods to quantitatively analyze relevant processes, and explore the impact of various factors on the transport process, thereby elucidating the underlying mechanisms of dual lymph node transfer strategy because of the deformability of Pickering emulsion, and providing guidance for the design of Pickering emulsions.

1.3.3 Current state of research

Despite the potential of deformable Pickering emulsions in vaccine delivery, both experimental and simulated studies on this topic remain sparse. In terms of experiments, with the size of the cell gap ranging from 20 to 100nm, it is difficult for solid particles to pass through the cellular gaps and concentrate within the lymph nodes [32]. As an alternative strategy, Song et al. explored the deformability of albumin-stabilized Pickering emulsion [4]. Though, the size of the emulsion droplet (~330 nm) is larger than 3 times the intercellular gap, the cell-mimic deformability granted the droplets to attach and squeeze themselves between the cell gaps under the interstitial flow and

adjust droplet size to cross the endothelial cell gap. This allows the deformable Pickering emulsion to achieve high lymph node retention of the vaccines and induces increased immune activations. Therefore, the quantitative analysis and mathematic models are expected to elucidate the process details and offer implications to optimize novel Pickering emulsions with higher lymph node transport efficiency and immunogenicity.

In terms of simulation, no direct relevant research has been found yet, now. Recent advances, such as the simulation work [33] and other related work [34–36]have showcased the potential of multiscale modeling and dissipative particle dynamics (DPD) in understanding the behavior of biological systems and inspire the simulation of this research. The CRUNCH group developed a red blood cell model that has deformable viscoelastic membranes that show rheological response and hydrodynamics behavior based on the dissipative particle dynamics simulation method. Later, this model shows some potential in other related areas such as cellular movement in confined spaces and the process of nanoparticle endocytosis by the cell membrane.

1

Chapter 2 Mathematical framework of dissipative particle dynamics simulation for the cellular tissues

Natural systems can be characterized at different scales, including microscale, mesoscale, and macroscale [37]. Microscale involves dimensions and timescales at the nanometer and nanosecond levels, governed by the laws of quantum or classical mechanics [38,39]. The macroscale refers to phenomena that can be directly observed and quantified, characterized by continuous partial differential equations like the Navier-Stokes equations in fluid mechanics [40]. Mesoscale, situated between the micro and macro realms, typically focuses on the order of micrometers and microseconds, involving systems like colloidal suspensions, polymer solutions, and biological membranes, which are categorized as complex fluids.

Complex fluid systems are crucial in industrial technology, especially within biological and biomedical sciences, for applications like lab-on-a-chip devices, separators, and drug delivery mechanisms. In contemporary science, computer simulations, particularly Molecular Dynamics, are essential for the mathematical modeling of these natural systems. However, due to computational cost limitations, MD is primarily applicable to microscale simulations.

To surmount the challenges of using macroscale PDEs for mesoscopic phenomena, methods like Computational Fluid Dynamics (CFD) [41] have emerged. Though adept for large-scale events, these techniques cannot fully represent mesoscale fluid behavior, missing out on the microstructure and randomness. Enter mesoscopic simulations like Dissipative Particle Dynamics (DPD), which marry MD's Lagrangian aspects with Lattice-Gas Automata's scale considerations [42]. DPD outpaces MD and surpasses

LGA in versatility, having matured into a robust framework with refined models and algorithms, thus enhancing complex fluid simulations. DPD's theoretical underpinnings have been thoroughly investigated through both macro-to-meso and micro-to-meso lenses.

2.1 Dissipative particle dynamics

Dissipative Particle Dynamics (DPD) is a simplified molecular dynamics approach where each particle symbolizes a group of molecules, interacting through conservative, dissipative, and random forces [43,44]. This model adheres to the coarse-graining process previously outlined, with the movement of each particle governed by Newton's second law, thereby establishing the particles' equations of motion:

$$\frac{d\mathbf{r}_i}{dt} = \mathbf{v}_i \tag{1}$$

$$m_i \frac{d\mathbf{v}_i}{dt} = \sum_{i \neq i'} (\mathbf{f}_{ii'}^{\mathrm{DPD}} + \mathbf{f}_e) \tag{2}$$

m_i is the mass of particle i, which is generally set to 1 to simplify the calculation. $\mathbf{f}_e$ is the additional extra force that is exerted on the particle. The force $\mathbf{f}_{ii'}^{\mathrm{DPD}}$ is divided into three parts: conservative force $\mathbf{f}_{ii'}^{C}$, dissipative force $\mathbf{f}_{ii'}^{D}$ and random force $\mathbf{f}_{ii'}^{R}$.

The conservative force is

$$\mathbf{f}_{ii'}^{C} = a_{ii'} w^{C}(r_{ii'}) \tag{3}$$

The dissipative force is

$$\mathbf{f}_{ii'}^{D} = \sum_{i \neq i'} -\gamma_{ii'} w^{D}(r_{ii'})(\mathbf{e}_{ii'} \cdot \mathbf{v}_{ii'})\mathbf{e}_{ii'} \tag{4}$$

The random force is

$$\mathbf{f}_{ii'}^{R} = \sum_{i \neq i'} \sigma_{ii'} w^{R}(r_{ii'}) \theta_{ii'} \mathbf{e}_{ii'} = \sum_{i \neq i'} \sigma_{ii'} w^{R}(r_{ii'}) \zeta_{ii'} \Delta t^{-\frac{1}{2}} \mathbf{e}_{ii'} \tag{5}$$

The conservative force acts as a soft potential along the center-to-center distance between particles, representing the chemical properties of the DPD system. It is derived from pairwise interaction potentials between neighboring particles, where $a_{ii'}$ is the

repulsive force parameter that determines the strength of their collisions. $w^C(r_{ii'})$is the conservative force weight function, which is generally the standard weight function $w^C(r_{ii'}) = 1 - \frac{r_{ii'}}{r_c}$. Where， $r_{ii'}$ is the interparticle distance, $\mathbf{r}_{ii'} = \mathbf{r}_i - \mathbf{r}_{i'}$， $r_{ii'} = |\mathbf{r}_{ii'}|$ and r_c is the truncation radius, which indicates the effective range of force exerted between particles and is usually considered as the unit length, i.e.,$r_c = 1$. $\mathbf{e}_{ii'}$ denotes the unit vector between particle i and particle j, taken as $\mathbf{e}_{ii'} = \frac{\mathbf{r}_{ii'}}{r_{ii'}}$, with the direction from i' to i. The conservative force is fluid/system dependent as a whole.

Essentially, the dissipative force is a kind of frictional force and represents viscous resistance with the fluid, which could account for energy loss. $\gamma_{ii'}$ is intensity controlling parameter and $w^D(r_{ii'}) = 1 - \frac{r_{ii'}}{r_c}$, is weight function of dissipative force. The negative symbol represents the direction of force exerting on a pair of particles is opposite from their relative velocity. Furthermore, $\mathbf{f}_{ii'}^D$ is proportional to the $\mathbf{v}_{ii'}$, which illustrate that the more value of $\mathbf{v}_{ii'}$, the more viscous resistance between a pair of particles.

The random force weight function $w^R(r_{ii'})$ is to be chosen as the formula $w^R(r_{ii'}) = \left(1 - \frac{r_{ii'}}{r_c}\right)^{m^R}$. In the standard DPD method, the parameter m^R was initially fixed at 1. However, varying the exponent values allows for the adjustment of fluid viscosity, consequently leading to an increase in the Schmidt number [45,46]. The random force is a stochastic part of interaction between dissipative particles and makes up for lost degrees of freedom eliminated after the coarse-graining in order to prevent the tendency that the system is cooling down with only dissipative force interaction.

According to the fluctuation-dissipation theorem [47], temperature regulation is realized by striking a balance between random and dissipative force and we can obtain

the relationship of the dissipative force weight function $w^D(r_{ii'})$ and $w^R(r_{ii'})$, dissipative forces coefficient $\gamma_{ii'}$ and random forces coefficient $\sigma_{ii'}$:

$$w^D(r) = [w^R(r_{ii'})]^2, \sigma_{ii'}^2 = 2\gamma_{ii'}k_BT \quad (6)$$

where T is the temperature and k_B is the Boltzmann constant. By the way, the dissipative and random forces constitute the thermostat of DPD.

More than the cutoff r_c, the interparticle force of particles vanishes to zero. According to the view of fluid particle model [48] and single dissipative-particle-dynamics particles model [35,49,50], we could consider a DPD particle to represent one real particle in the simulation.

In summary, by employing reduction and coarse graining of discrete atoms in the Molecular Dynamics, the representation of fundamental particles in the DPD method is formed. Interatomic forces in MD are reduced to conservative forces in DPD. Furthermore, dissipative forces and random forces are introduced to characterize viscosity dissipation behavior and the continuous irregular random motion that becomes significant at the mesoscale relative to the macroscale. Figure 10 describe the coarse-grained dissipative particle's representation and effect of different basic force.

The DPD method has been verified by simulating Lennard-Jones fluid with molecular dynamics method and Navier-Stokes equation. The simulation result shows good aggrement with equilibrium simulations, Couette flow simulations, Poiseuille flow simulations by different methods. [51]

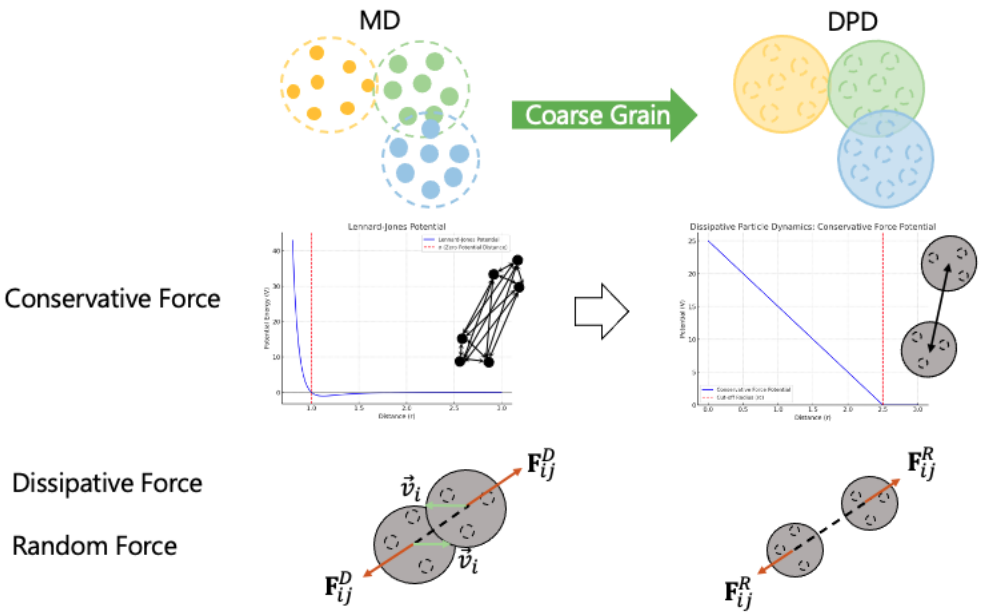

Figure 10 The illustration of representation of basic particle for dissipative particle dynamics method and effects of different forces

2.2 Mesoscale viscoelastic membrane model

2.2.1 Introduction of MVMM

The mesoscale viscoelastic membrane model has evolved from the development of mesoscale models for red blood cells, whose membrane consists of a lipid bilayer supported by an internal cytoskeleton. The cytoskeleton, composed of a compact network of spectrins and actins, provides structural stability. The properties including viscosity, elasticity, and bending stiffness, are concluded from the physical properties of these biological components. The development process for this model is summarized as follows: First, a spring-based crosslinked network membrane model was initially introduced and subsequently refined as a discrete representation of hemoglobin at the protein level [52,53]. Secondly, building on this foundation, a systematic coarse-graining method was crafted, considerably reducing the number about the number of independent variables [54]; Thirdly, the simplified model is further optimized to deliver accurate mechanical responses [55]; Fourth, this spring-based crosslinked network

model has more applications in some similar fields, such as the deformation and marginalization of white blood cells [56], modeling rigid nanoparticles in the simulation of their evolution in endocytosis within the cell membrane [34], even the simulation of complete blood flow [57]. In addition, the mesoscale viscoelastic membrane model is constantly evolving, not only in combination with standard dissipative particle dynamics (DPD) methods but also extending to coarse-grained molecular dynamics (CGMD) [58], lattice Boltzmann method (LBM) [59] , and transport dissipative particle dynamics (tDPD) [60] mesoscale numerical simulation methods.

2.2.2 Numerical model

The cell membrane model consists of a set of vertices (DPD particles) and the two-dimensional triangular network they form, with the N_v vertices interconnected to form N_s edges and subsequently N_t triangles. The total energy describing the triangular network model could be divided into four different parts, such as in-plane elastic viscous dissipative energy, bending energy, surface area energy, and volume energy, which are labelled by U_{IP}, U_B, U_A, U_V respectively [61].

$$U(\{\mathbf{r}_i\}) = U_{IP} + U_B + U_A + U_V \tag{7}$$

The in-plane energy is given by the following equation:

$$U_{IP} = \sum_{j=1}^{N_s}\left[U_{IPS}(l_j) + U_{IPV}(\Delta v_j)\right] + \sum_{k=1}^{N_t}\frac{C_q}{A_k^q} \tag{8}$$

In the equation, IPS and IPV represent the in-plane spring energy and the in-plane viscous dissipation, respectively. The first summation term in the equation expresses the contribution of the viscous springs; $l_j$is the length of the j-th spring, and $\Delta v_j$is the difference in relative velocities at the ends of the spring. The second term represents the summation of the elastic energy stored in each triangular piece of network segment from the physical viewpoint, where A_K is the area of the k-th triangle.

A more concise and intuitive model consisting of the potential energy of the worm-like chain (WLC) model and power function (POW) is adopted here. As shown in the following equation:

$$U_{IP} = \sum_{j=1}^{N_s} U_{WLC} + \sum_{j=1}^{N_s} U_{POW} = \sum_{j=1}^{N_s} \left[\frac{k_B T l_m \left(3x_j^2 - 2x_j^3\right)}{4p\left(1 - x_j\right)} + \frac{k_p}{(m-1) l_j^{m-1}} \right] \tag{9}$$

where, $x_j = \frac{l_j}{l_{max}} \in (0,1)$, where l_{max}, p, k_p and m represent the maximum spring extension, the persistence length, the spring constant, and the specified exponent, respectively. The attractive forces exerted by the WLC springs cause the components to contract. The force produced by POW model can neutralize the contractility of the triangular surface bases. The combined action of both can generate an equilibrium spring length and, in this way, p and k_p can be obtained from the relationship of the related parameters from WLC model and the selected exponent n. At this point, the stored elastic energy can be ignored and C_q can be set to 0 [61].

The bending energy is concentrated on the edges of the two adjacent neighbor triangular segments from each other to maintain cell shape and resist bending deformation, and the bending potential energy is shown as follows:

$$U_B = \sum_{j=1}^{N_s} k_b \left(1 - \cos\left(\phi_j - \phi_0\right)\right) \tag{10}$$

where k_b, ϕ_j and ϕ_0 are the bending modulus, the instantaneous angle between two adjacent triangles sharing a common edge j, and the spontaneous angle, respectively.

In equations 7, the last two terms represent the conservation of the cell membrane area and the incompressibility of the internal fluid, respectively, by enforcing area and volume constraints to maintain the cell shape.

$$U_A = \frac{k_a}{2A_0^{tot}} (A - A_0^{tot})^2 + \frac{k_d}{2A_0} \sum_{k=1}^{N_t} (A_k - A_0)^2 \tag{11}$$

$$U_V = \frac{k_v}{2V_0^{tot}} (V - V_0^{tot})^2 \tag{12}$$

where, k_a, k_d, k_v, A, V, A_0^{tot} and V_0^{tot} are the constraint coefficients of the global area, constraint coefficients of the local area, constraint coefficients of volume, the instantaneous total area, total volume, the specified total area, and total volume, respectively.

The forces $\mathbf{f}_i^{\mathrm{MVMM}}$ on the nodes can be obtained by taking the derivative of the elastic network energy:

$$\mathbf{f}_i^{\mathrm{MVMM}} = -\frac{\partial U(\{\mathbf{r}_i\})}{\partial \mathbf{r}_i} \tag{13}$$

2.2.3 Membrane mechanical properties

According to the analysis for a node in a segment of a two-dimensional hexagonal network of equilateral triangles and the virial theorem [62–65], the Cauchy stress at node **v** is obtained by the following equation in the research :

$$\begin{aligned}\tau_{\alpha\beta} = -\frac{1}{S}\left[\frac{f(r_1)}{r_1} r_1^{\alpha} r_1^{\beta} + \frac{f(r_2)}{r_2} r_2^{\alpha} r_2^{\beta} + \frac{f(|\mathbf{r}_2 - \mathbf{r}_1|)}{|\mathbf{r}_2 - \mathbf{r}_1|}\left(r_2^{\alpha} - r_1^{\alpha}\right)\left(r_2^{\beta} - r_1^{\beta}\right)\right] \\ - \left(q\frac{C_q}{A_k^{q+1}} + \frac{k_a(A_0^{tot} - N_t A)}{A_0^{tot}} + \frac{k_d(A_0 - A)}{A_0}\right)\delta_{\alpha\beta}\end{aligned} \tag{14}$$

where， α and β represent x or y, $f(r)$, N_t, $\delta_{\alpha\beta}$ and S are the spring force, the total number of triangles, the Kronecker delta, and the area of the hexagonal element centered at **v**, respectively. $A_0^{tot} = N_t A_0$

2.2.3.1 Shear modulus

The shear modulus can be represented as $\mu_0 = \left.\frac{\partial \tau_{xy}}{\partial \gamma}\right|_{\gamma=0}$, which can be obtained by taking the derivative of the stress tensor with respect to the applied shear strain γ.

$$\mu_0 = \frac{\sqrt{3}k_B T}{4pl_m x_0}\left(\frac{x_0}{2(1-x_0)^3} - \frac{1}{4(1-x_0)^2} + \frac{1}{4}\right) + \frac{\sqrt{3}k_p(m+1)}{4l_n^{m+1}} \tag{15}$$

2.2.3.2 Compression modulus

The elastic area compression modulus K is derived from calculating the in-plane pressure against the area contraction, and the pressure is given by the following equation:

$$p = -\frac{1}{2}(\tau_{xx}+\tau_{yy}) = \frac{3l}{4A}f(l) + q\frac{C_q}{A_k^{q+1}} + \frac{(k_a+k_d)(A_0-A)}{A_0} \tag{16}$$

The compression modulus K is then defined as:

$$K = -\frac{\partial P}{\partial \log(A)}\Big|_{A=A_0} = -\frac{1}{2}\frac{\partial P}{\partial \log(l)}\Big|_{l=l_0} = -\frac{1}{2}\frac{\partial P}{\partial \log(x)}\Big|_{x=x_0} \tag{17}$$

$$K = \frac{\sqrt{3}k_BT}{4pl_m(1-x_0)^2}\left[\left(q+\frac{1}{2}\right)(4x_0^2-9x_0+6) + \frac{1+2(1-x_0)^3}{1-x_0}\right] + k_a + k_d \tag{18}$$

$$K = 2\mu_0 + k_a + k_d \tag{19}$$

Furthermore, we can obtain the Young's modulus and Poisson's ratio as:

$$Y = \frac{4K\mu_0}{K+\mu_0}, Y \to 4\mu_0, if\ K \to \infty \tag{20}$$

$$\nu = \frac{K-\mu_0}{K+\mu_0}, \upsilon \to 1, if\ K \to \infty \tag{21}$$

In practice, we use values of $\mu_0 = 100$ and $k_a + k_d = 5000$, which produce a Young's modulus of the approximately incompressible membrane about 2% less than its asymptotic value of $4\mu_0$ [61].

2.2.3.3 Bending rigidity

The connection between the bending modulus k_b and the macroscopic membrane bending stiffness k_c can be deduced from a hypothesis of spherical shell. By equating the macroscopic bending energy and E_B, and deriving the spontaneous angle ϕ_0 based on the number of the whole nodes N_v on the spherical surface, we obtain:

$$k_b = \frac{2}{\sqrt{3}}k_c, \theta_0 = \cos^{-1}\left(\frac{\sqrt{3}(N_v-2)-5\pi}{\sqrt{3}(N_v-2)-3\pi}\right) \tag{22}$$

2.2.3.4 Membrane viscosity

For the membrane viscosity aspect of the mesoscale viscoelastic membrane model, the influence of original DPD dissipative force and random force is insufficient. Referring to the fluid particle model [48], the dissipative force term in standard DPD is modified as [61]:

$$\mathbf{f}_{ij}^{D} = -\gamma^{T}\mathbf{v}_{ij} - \gamma^{C}\left(\mathbf{v}_{ij}\cdot\mathbf{e}_{ij}\right)\mathbf{e}_{ij} \tag{23}$$

The first term in the equation provides the dominant viscous contribution, while the second term is similar with the dissipative force of standard DPD. γ^{T} γ^{C} are dissipative coefficients. According the general fluid particle model and the fluctuation-dissipation relationship, the random force is adjusted accordingly and the details of calculation could be found in software [60,66]. The shear stress τ_{xy} over a brief period can be estimated based on the contribution of the dissipative force in the aforementioned equation.

$$\tau_{xy} = \dot{\gamma}\left(\gamma^{T} + \frac{1}{4}\gamma^{C}\right) \tag{24}$$

where, $\dot{\gamma}$ is the constant shear rate. Hence, the membrane viscosity is:

$$\eta_{m} = \frac{\tau_{xy}}{\dot{\gamma}} = \sqrt{3}\left(\gamma^{T} + \frac{1}{4}\gamma^{C}\right) \tag{25}$$

This equation indicates that γ^{T} constitutes a major part of membrane dissipation. Consequently, the numerical outcomes exhibit minimal sensitivity to the value of γ^{C}. Given the elevated values of γ^{C} might induce numerical instability in the simulations, it is often set to the minimum value of $\frac{1}{3}\gamma^{T}$ [61].

2.2.4 Unit scaling analysis

In the development of a coarse-grained cellular model, the physical quantalities and parameters of DPD model in model must be scaled with physical units. The length scale factor λ is based on the characteristic length at equilibrium, L_0^M, which is chosen the form as diameter in this work, where $[L_0^M] = \lambda$ and the M represents model units. λ can be obtained by the following formula:

$$\lambda = \frac{L_0^P}{L_0^M}[m] \tag{26}$$

where $[m]$ represents meters.

The young's modulus(2D) is utilized for an additional input parameter for energy scaling process. An energy scaling factor ξ is obtained by dimensional analysis of Young's modulus Y:

$$\xi = (k_B T)^M = \frac{Y^P}{Y^M}\left(\frac{L_0^P}{L_0^M}\right)^2 [J] = \frac{Y^P}{Y^M}\left(\frac{L_0^P}{L_0^M}\right)^2 (k_B T)^P \tag{27}$$

where, $[J]$ denotes joules and $k_B T$ represents a unit of energy from Boltzmann's constant and temperature in the field of thermodynamics and statistical mechanics. Furthermore, force scaling factor ε and pressure scaling factor ν can be obtained by:

$$\varepsilon = \frac{Y^P}{Y^M}\frac{L_0^P}{L_0^M}[N] = \frac{\xi}{\lambda}[N] \tag{28}$$

$$\nu = \frac{\xi}{\lambda^3}[Pa] \tag{29}$$

Based on dimensional analyses of viscosity η and Newton's second law, time scaling factor τ and mass scaling factor μ can be calculated as follows:

$$\tau = \frac{\eta^P}{\eta^M}\frac{Y^M}{Y^P}\frac{L_0^P}{L_0^M}[s] \tag{30}$$

$$\mu = \frac{Y^P}{Y^M}\tau^2[kg] \tag{31}$$

where $[s]$ denotes second and $[kg]$ denotes kilogram.

2.3 The relationship of different concepts for the mathematic framework

In summary, the Dissipative Particle Dynamics (DPD) method can indeed be considered an application of Lagrangian mechanics where the dynamics of a system are typically described by tracking the time evolution of each particle's position and momentum.

The relationship of different concepts of the framework in this research is shown in Figure 11. The standard DPD method offers a basic framework to describe the dynamical property of an indivisible particle, which naturally involves how to represent the interaction between particles and how to iterate over the dynamic behavior under the constraints of the thermostat. Additionally, as dissipative particles are a coarse-grained abstraction, their dimensional selection is arbitrary. Therefore, it is essential to clearly define the mapping relationship from the real entities to reductive particles. In addition to the dissipative and random forces that describe energy dissipation processes and irregular Brownian motion at the mesoscale, other interactions are abstracted and simplified as conservative forces. To characterize the dynamic behavior of cells (a group of dissipative particle clusters), the interactions among dissipative particle clusters are categorized and the originally singular conservative force between dissipative particles is enhanced. Thus, the dynamic evolution of dissipative particles is conducted under the constraints of macroscopic mechanical properties. In addition to the viscosity of particles induced by dissipative and random forces (Within the scope of single-particle DPD in this study), the material mechanical properties of the entities represented by the clusters of dissipative particles are obtained by solving the relationship between the discrete particles' virial stress and the Cauchy stress.

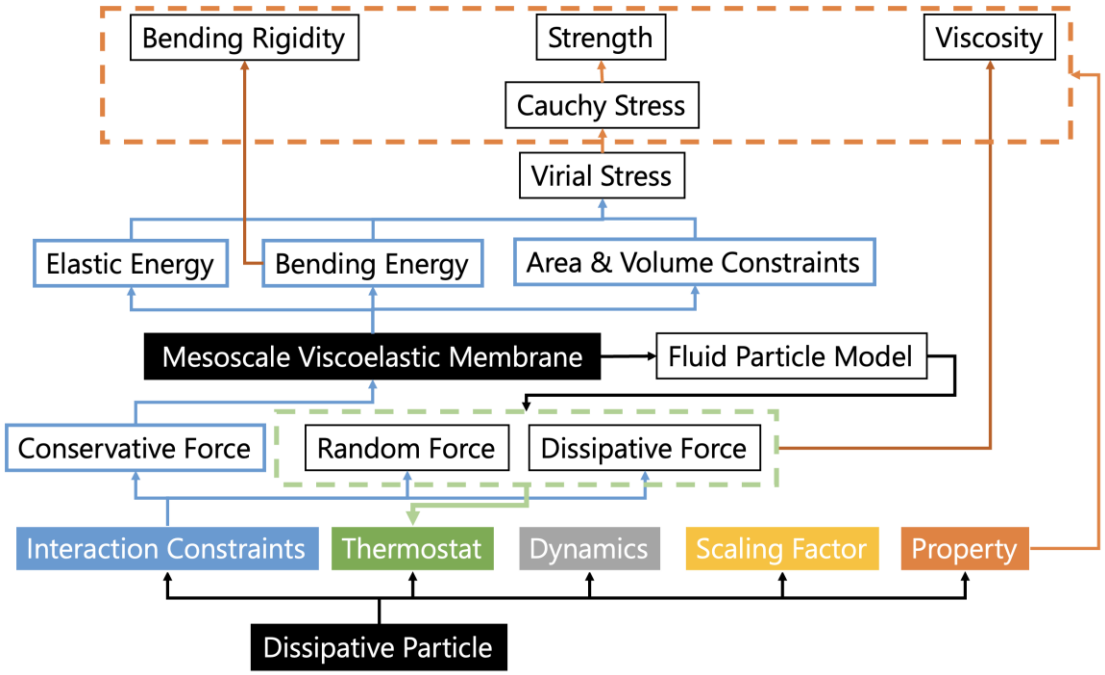

Figure 11 The Relationship of Different Concepts

Given that the focus of this project is on the transport processes in drug delivery methods, the research is centered on describing the kinetic transfer processes. Therefore, the theoretical framework of this project is primarily situated within the theoretical system of the Dissipative Particle Dynamics (DPD) method, which adheres to the conservation of momentum. Additionally, the standard DPD theory has been further developed to include energy conservation and mass conservation, leading to the emergence of the energy-conserving DPD (eDPD) method [67] and the transport DPD (tDPD) method [68].

2.4 Summary

The development of a dissipative particle dynamics framework provides a valuable computational tool for simulating cellular tissues at the mesoscale. By effectively bridging the detailed molecular interactions and the broader, continuous fluid dynamics,

DPD enables the exploration of complex fluids within biological and biomedical contexts with greater computational efficiency.

The framework's strength lies in its ability to reduce computational load without sacrificing the essential physics of mesoscale phenomena. Using conservative, dissipative, and random forces, the DPD model captures the nuanced behaviors of mesoscale systems, including the thermal and viscous effects crucial for realistic simulations.

In summary, the DPD simulation framework represents a significant advance in the modeling of natural systems, especially in the field of drug delivery. It stands as a robust approach to understanding the complex interactions within cellular environments, paving the way for future innovations in the simulation and analysis of biological systems.

Chapter 3 Cell modeling

3.1 Introduction

Figure 12 provides a visual comparison of the hierarchical structures in a biological system ranging from tissue to molecular levels, coupled with an illustration of the coarse-graining technique. Coarse graining is a computational strategy for simplifying complex biomolecular models by reducing the degrees of freedom. It involves aggregating multiple atoms or molecular details into larger representative units (coarse grains) to streamline simulations. The figure displays, from left to right, tissue-level organization (as exemplified by blood tissue), cell-level structure (represented by a red blood cell), subcellular architecture (cellular network structures), macromolecular complexity (protein complex) [69], and their respective coarse-grained models. This visualization underscores the significance of cross-scale analysis in biological research, particularly for comprehending intricate biological processes and developing therapeutic interventions.

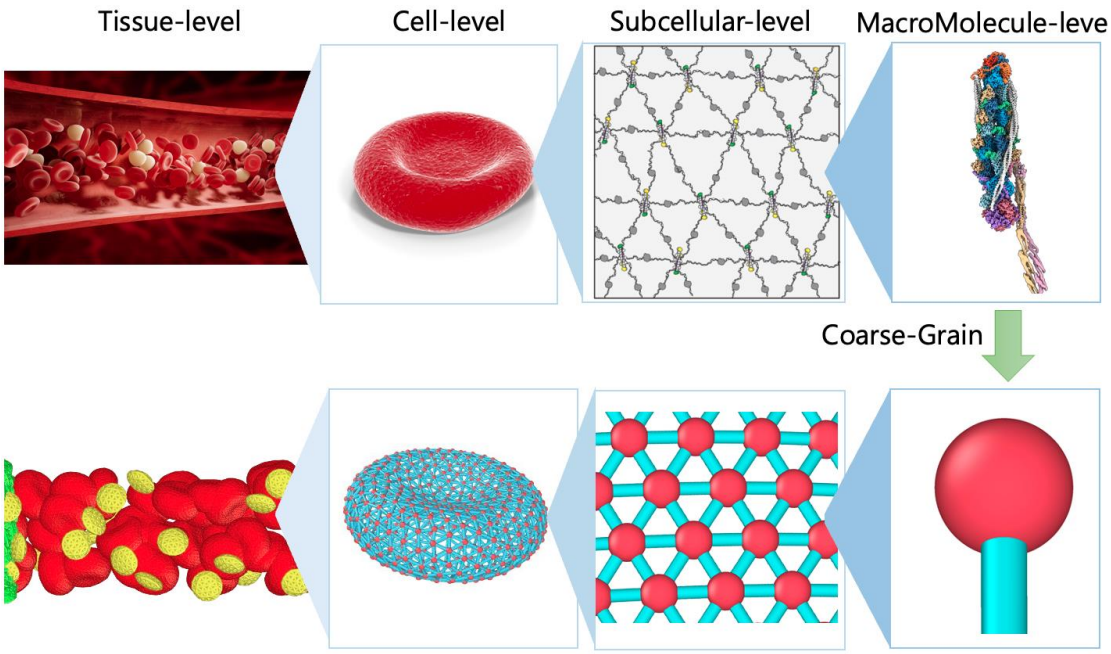

Figure 12 Visual representation of biological hierarchy and coarse-graining approach

The cytoskeleton refers to the fibrous network structure present within biological cells, primarily composed of cytoplasmic filamentous proteins. The cytoskeleton is not a static structure but is dynamically remodeled. As a load-bearing architecture, the cytoskeleton assists in maintaining cellular shape and structure, providing resistance against external forces that may compromise cell integrity; it exerts forces on the surrounding matrix and plays a pivotal role in the mechanical sensing mechanisms of the cell.

Erythrocytes exhibit a high degree of deformability yet possess stable mechanical properties capable of withstanding substantial shear stress. Their robust mechanical performance is attributed to the spectrin-actin membrane skeleton, a quasi-hexagonal cytoskeletal network formed underneath the bilayer. This network, or "nodal" structure, consists of interconnected long and flexible $(\alpha_1\beta_1)_2$ spectrin tetramers linked by short actin filaments (F-actin) complexes, creating a two-dimensional lattice. The mechanical properties of the cytoskeleton are reflected by this planar network structure in three-dimensional space. The schematic diagram is shown in Figure 13. Based on the

mesoscale viscoelastic membrane model and the structure of cytoskeleton, actin is mapped to a Dissipative Particle Dynamics (DPD) particle, while the extensibility of $(\alpha_1\beta_1)_2$ spectrin can be characterized by a worm-like chain model and is represented as a bond between DPD particles.

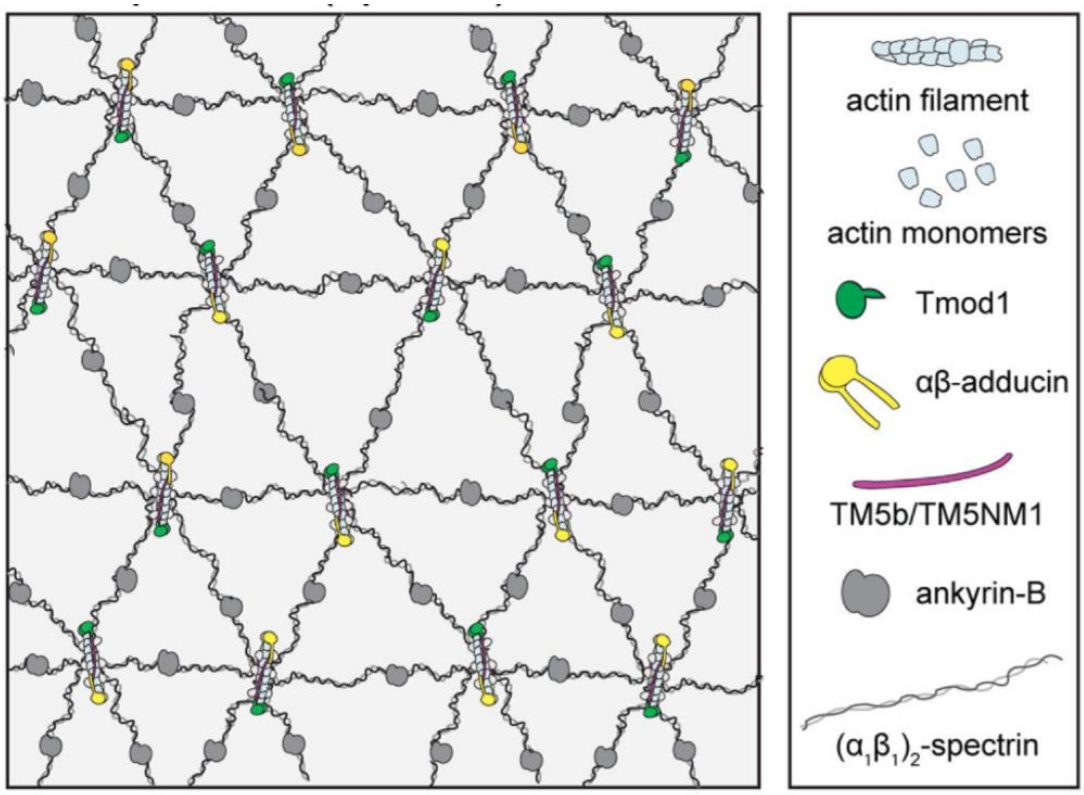

Figure 13 Membrane skeleton organization in RBCs [70]

The cytoskeleton, composed of actin and spectrin, is not exclusively situated on the membrane of erythrocytes; its reticular structure is also extensively present across various other cell types, such as nerve cells [28], immune cells, and so on. As for the endothelium cells, the cytoskeleton is primarily composed of spectrin and its binding proteins including F-actin, and shows a similar structure to red blood cells [71]. As for the skeletal muscle fiber, sarcolemma is the outlet membrane of the skeletal muscle cell (muscle fiber) and is equivalent to the cell membrane in other cell types. It envelops muscle fibers and is closely associated with them. The sarcolemma directly surrounds muscle fibers, isolating them from the external environment. Internally, the sarcolemma is attached to a fine network structure known as the basement membrane, which

enhances the stability of muscle fibers. SEM shows that actin and spectrin exit in the sarcolemma[30]. As for the innate immune cells such as myeloid cells including macrophages, dendritic cells, and granulocytes, generate large membrane protrusions, which are broadly referred to as ruffles [72,73]. The cortex of myeloid cells is characterized by a dense network of isotropically distributed F-actin and spectrin is distributed between actins.

To streamline the model, this study omits the intracellular cytoskeletal components other than the cell membrane. Additionally, constraints on the surface area and volume are incorporated into the mesoscale viscoelastic membrane model to mitigate the impact of omitting these components. The tetrameric lattice structure in two dimensions exhibits favorable mechanical responsiveness and equivalence, hence this study uniformly employs this architecture to represent cells.

The unique properties of the cytoskeleton necessitate specific requirements for mesh model construction: The mesh must accurately represent the complex architecture of the cytoskeleton, encompassing the diverse cellular shapes and the connectivity of grid points; A two-dimensional surface model within a three-dimensional space must be established; The distances between grid points should be approximately equal, fulfilling both the requirements of spectrin and ensuring the stability of the model.

3.2 Mesh generation method

The DistMesh algorithm [74,75] is a mesh generation tool based on the principles of distance functions and adaptive mesh density. Utilizing Delaunay triangulation, it optimizes nodes through a force-based smoothing process, yielding high-quality meshes suitable for simulating complex geometrical structures. The principal advantage of the DistMesh algorithm lies in its flexibility and efficiency, particularly evident when

handling biomedical models with intricate surfaces, as it can produce meshes with appropriate density and uniform distribution.

SDF stands for "Signed Distance Function," a mathematical and computer graphics concept that describes the shortest distance from a point to a surface or shape. The value at each point in an SDF represents the distance to the nearest surface, with positive values indicating a position outside the surface, negative values indicating a position inside, and zero typically representing a position exactly on the surface. Therefore, the complicated shape of the cell could be constructed by DistMesh algorithm.

3.3 Evaluating Results of Generated Mesh

To represent the quality of mesh generation, the following criteria have been selected: The minimum mesh quality, expressed as the ratio of area to perimeter, where the ideal mesh elements are equilateral triangles, at which point the ratio of area to perimeter is maximized; The coefficient of variation of area, the standard deviation of the area of mesh elements relative to the average area, is used to describe the degree of variation in the area relative to the average area, where a smaller value indicates a more uniform distribution of mesh element areas; The proportion of nodes with different connectivities, for a two-dimensional tetrahedral planar mesh, the higher the proportion of nodes with six connectivities, the better.

For the cell types and their morphological characteristics involved in this study, cellular mesh models of various shapes have been constructed, including capsule (muscle fiber), concave (red blood cell), ellipsoid (flap of a lymphatic endothelial cell), leaf (lymphatic endothelial cell), and sphere (dendritic cell). In addition to the parameters of cell morphology, the distance between nodes serves as an independent variable in the mesh generation process.

The mesh results for different shape cells are listed in Appendix 1. In summary, the results indicate that the distribution of nodes exhibits a commendable level of uniformity. The comparatively symmetrical triangles align well with the requirements for a two-dimensional tetrameric lattice of the cytoskeleton, suggesting suitability for representing the cellular framework. The different shapes of cell models are shown in Figure 14

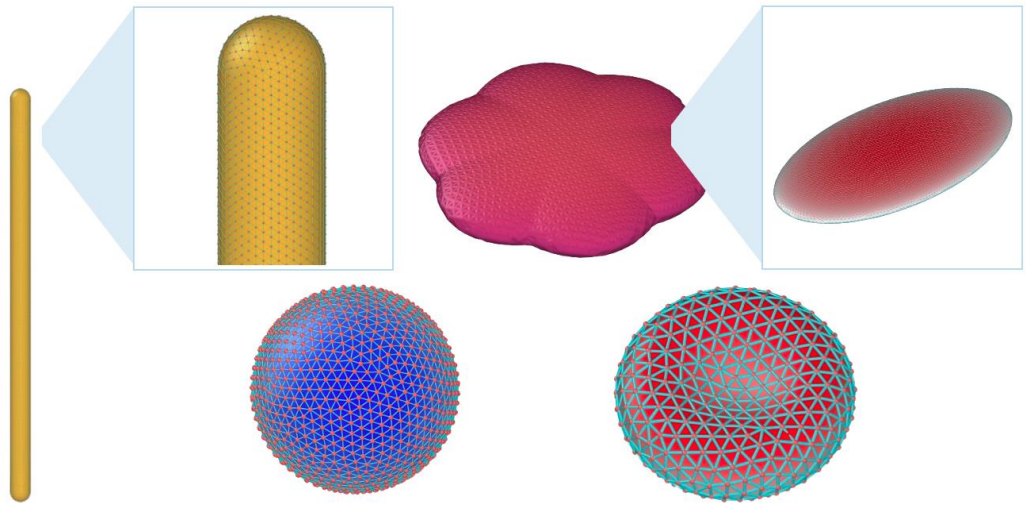

Figure 14 Different shapes of cell

3.4 Validation of cellular properties

Molecular mechanics experimental techniques are instrumental in the study of mechanical properties at the molecular and cellular levels, crucial for understanding biological processes. These techniques facilitate the elucidation of how biological molecules respond to mechanical forces, a key factor in signaling transduction mechanical work, and molecular interactions within cells. Their significance extends to disease research, particularly in understanding the molecular basis of diseases like

cancer and genetic disorders, where alterations in cellular mechanical properties are often implicated [76,77].

Relevant techniques include: atomic force microscopy (AFM), which employs a sharp probe to measure surface forces; optical tweezing, which exerts force on cells by driving photons to capture microbeads attached to the cell surface; micropipette aspiration, wherein gentle suction is applied to a micropipette placed on the cell surface, causing the cell to deform; and magnetic twisting cytometry, which uses a magnetic field to manipulate magnetic beads attached to the cell surface and so on [78].

To validate the mechanical performance of the constructed model, a simulation of optical tweezer experiments was conducted and compared with experimental data. Two high-refractive-index beads were tethered along the diameter axis at the two ends of the cell, and these beads could be separated from each other using laser light. By finely adjusting the optical trapping force and documenting the alterations in shape through an optical microscope, changes in the cell's axial and transverse diameters were measured in response to the stretching force applied. The optical tweezer stretching experiments are illustrated in Figure 15.

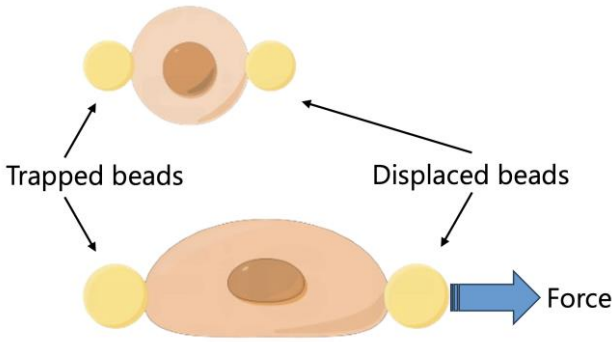

Figure 15 Schematic illustration of stretching test of the cell by optical tweezers

A model of a red blood cell with 500 particles was subjected to pulling forces at opposite ends to investigate its stretching deformation characteristics. Forces ranging from 0 pN to 200 pN were applied. The results of cell deformation under different forces are presented in Figure 16, and the corresponding axial displacements of stretching force and transverse displacements of the cell at various applied forces are summarized in Figure 17. The optical images and measured data of true red blood cell experiment results are shown in Figure 18 and Figure 17, respectively.

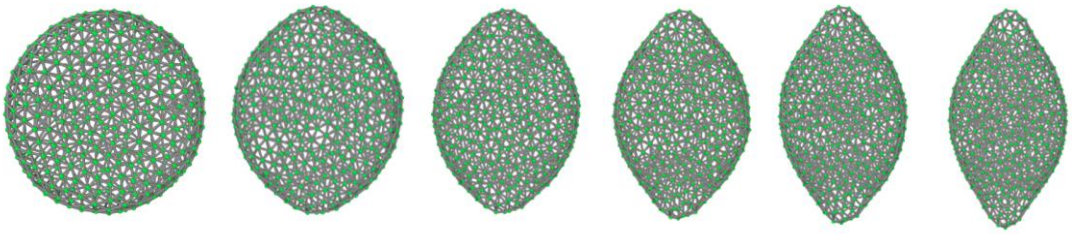

Figure 16 Deformation diagram of red blood cell under stretching force

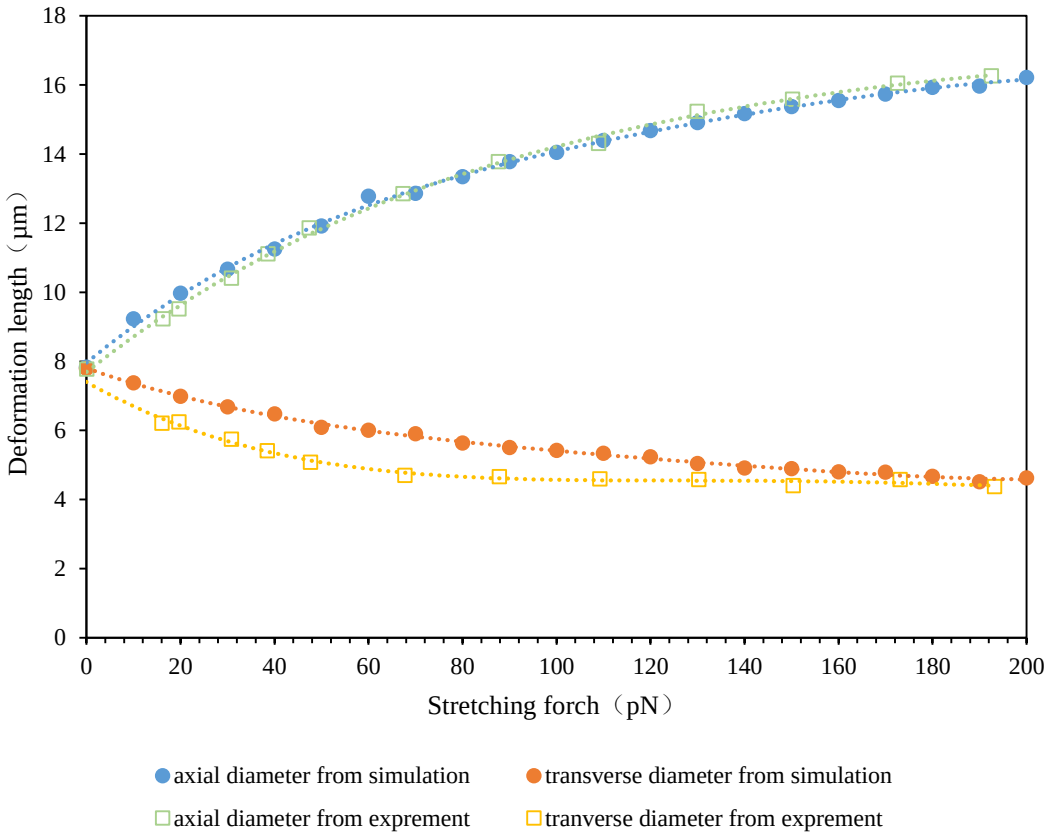

Figure 17 Deformation length of red blood cell under different stretching force. Explement data from [77]

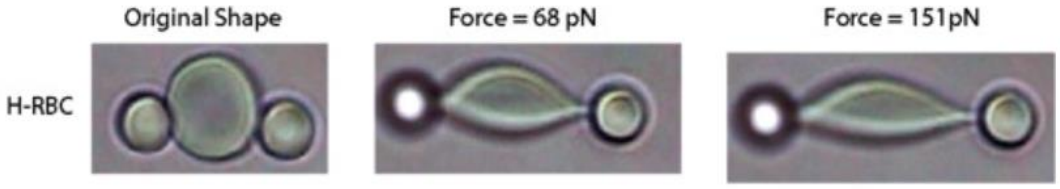

Figure 18 Optical images of healthy red blood cell under stretching forces [77]

The displayed graph provides an academic comparison between experimental and simulated biomechanical responses of red blood cells to stretching forces, showing an increase in axial diameter and a decrease in transverse diameter with rising force, and demonstrating the model's accuracy through the alignment of simulated and experimental data.

Some research studies have validated the accuracy of this model in aspects of fluid flow and dynamics through simulations such as red blood cell flow in the microfluid channel and examining their mechanics, rheology, and dynamics associated with the experiment results. [57,79]

3.5 Summary

In conclusion, this dissertation has successfully demonstrated the efficacy of a mesoscale viscoelastic membrane model in representing the mechanical behavior of the cytoskeleton across various cell types. By employing a coarse-graining approach, as visually summarized in Figure 12, we reduced the complexity of biological structures from the tissue level down to the macromolecular level, culminating in a computationally efficient representation that did not sacrifice the essential mechanical properties inherent to the cytoskeletal framework. This was particularly exemplified by the spectrin-actin membrane skeleton of erythrocytes, which exhibited remarkable mechanical stability under substantial shear stress, as delineated in our models and supported by empirical data.

The adoption of the DistMesh algorithm for mesh generation provided a flexible and robust method for constructing meshes that accurately reflected the complex architecture of the cytoskeleton and its mechanical responsiveness. The mesh quality, homogeneity of node distribution, and uniformity of element areas, as detailed in the Appendices, were critical to the model's success and demonstrated the utility of the DistMesh algorithm in creating geometries that conform to the intricate shapes of various cells.

The validation of the cellular models through the simulation of optical tweezer experiments and comparison with experimental stretching tests further reinforced the

model's reliability. The model capably replicated the deformation characteristics of red blood cells under stretching forces, providing insight into the cytoskeletal dynamics and the mechanical properties at play during cellular deformation.

Overall, this research encapsulated in thesis underscores the latent potential for computational modeling in augmenting understanding of cell mechanics. It paves the way for future investigations into the mechanical properties of cells and the role of the cytoskeleton. It provides robust tool and theory support for further observations of biological activity from the perspective of cellular organization.

Chapter 4 Transport phenomenon of Pickering emulsion in skeletal muscular tissue

4.1 Introduction

From the previous analyses of targeting lymph node transfer, we could find the possibilities of fluid pathways due to the physiological function and anatomical structures of lymph capillaries, besides the cellular pathway [23]. In this research, we investigate the transport process of Pickering emulsion in the skeletal muscular tissues first, furthermore, we integrate and produce a framework for 3-D cell modeling and dynamics analysis in cellular tissues.

Muscle cells, also known as muscle fibers, are observed within muscle tissues, specifically in skeletal muscles here. Morphologically, these cells are elongated and tubular in shape. Muscle fibers are essentially muscle cells and serve as the fundamental units of muscles. Each muscle fiber is composed of numerous myofibrils. Typically, the length of a muscle fiber ranges from a few millimeters to several centimeters (2-3 cm), with a diameter spanning approximately 10 to 100 micrometers [18,21]. For the Pickering emulsion, the diameter of the emulsion droplets ranges between 330nm and 500nm considered in this research [4,15].

4.2 Model simplification

In the consideration of simplifying the model, a uniform layer of cells is modeled to represent the process of flexible particles traversing the tissue layer of muscular cells.

Each cell is modeled as a capsule-like structure, which resembles the shape of muscle cells. The cells are uniformly sized and evenly distributed, with consistent intercellular gaps. The upper part of the cell layer is represented as the interior of the part of the muscle tissues. The flexible particles cross the cell gap from the upper part of the cell layer to the lower part of the cell layer, and this process is used to represent the process of the flexible particles crossing the part of the fascicle in the muscle tissue, thus allowing the Pickering emulsion to better carry out the next process to transport into the capillary of the immune system. The liquid filling the simulation box is modeled implicitly. To simplify the model and streamline the computational process, this study doesn't consider the adhesion between cells.

The entire simulation box is divided into the following order from top to bottom according to the actual physical model: boundary – free motion zone - fixed cell zone - free motion zone - boundary. The middle layer of the simulation box is set as a cell layer to represent the position of the intercellular matrix binding to the muscle cells by fixing the position of certain points on the cells, while the cells as a whole can maintain a certain viscoelasticity to show the morphological changes of the cells when the flexible particles cross the cell gap. The two sides of the simulated box immediately adjacent to the fixed cell zone are the free-motion zone, where the flexible particles move freely imposing additional constraints and additional forces. In the top free motion zone, new particles can be added at certain initial velocities, so that the flexible particles exhibit a top-to-bottom direction of motion. A layer of fixed DPD particles is set at the top and bottom of the box to indicate the boundary, which restricts the motion of the flexible particles to prevent them from crossing the boundary of the simulated box. The illustration is shown in Figure 19.

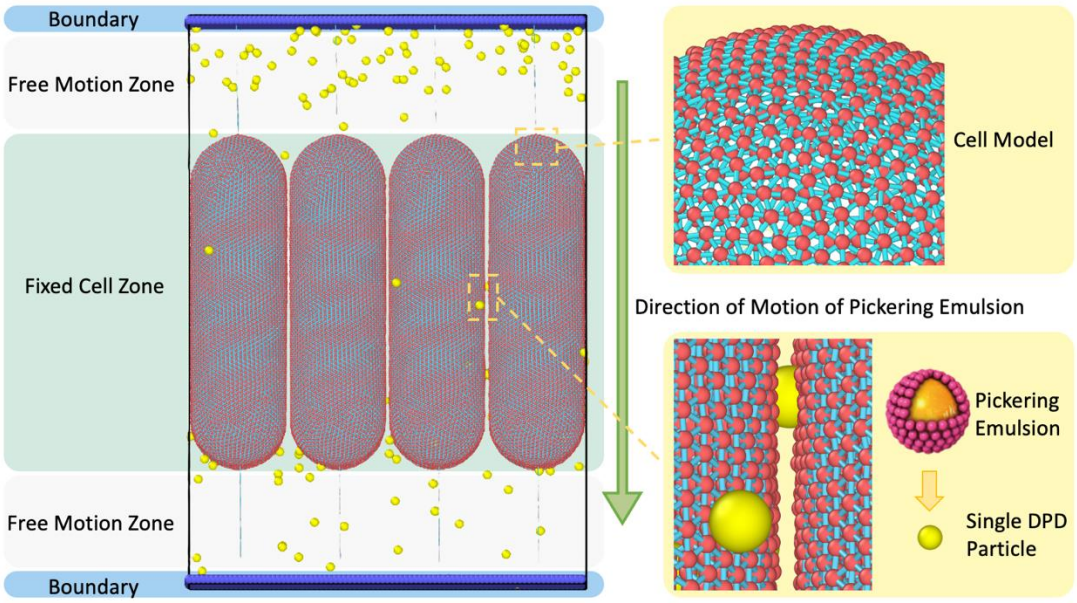

Figure 19 Illustration of the Simplified Model

Based on the morphological and mechanical properties analysis of cells and Pickering emulsions, the diameter of muscle cells is approximately 20 micrometers [18], with Young's modulus of about 12 kPa [80]. The Pickering emulsion has a diameter of around 500nm and a Young's modulus of approximately 36.5 MPa [4]. In this context, the Pickering emulsion can be considered as a rigid particle. Drawing on the triangular lattice spring network derived from hemoglobin modeling and rationalizing the process of flexible particles traversing the cell gap, a capsule-type layer of cells lined up side by side as the part of muscular tissue was constructed separately, and DPD particles were constructed represent the Pickering emulsion, and different viscoelastic parameters were set to reflect the different viscoelasticity between the cells and the particles. The cells are evenly distributed with the beads on the surface. Two neighboring beads create a bond element, three neighboring beads construct a triangular element, and a pair of triangular elements sharing a common edge constitute a bending element.

4.2.1 Extraction of physical quantities

To characterize the physical system of the model, it is necessary to first confirm the physical quantities in the real world, which are summarized in Table 1. L_0^P represents the characteristic length, where the diameter of muscle fibers is adopted as the characteristic length in this context, typically falling within the range of 10-100 micrometers [18]. The value of $(k_BT)^P$ is taken at the temperature T=296K. N_v^P and N_s^P represent the number of actins and spectrins in biology, respectively, but in the modeling process, a rough estimate was made, as the impact of different levels of coarse-graining on the mechanical properties and deformability of the cell is not pronounced [54]. Based on the finite element analysis, the result $Y^P = 3\mu_0^P$ was obtained, which aligns well with the experimental observations [81]. Here, the 'P' in the superscript stands for physical units.

Table 1 Physical Quantities in Physical Units

Physical Quantity		Value	
Symbol	Meaning	Cell	Droplet
L_0^P	Characteristic length	$20 \times 10^{-6}m$	$0.5 \times 10^{-6}m$
$(k_BT)^P$	Energy unit per unit particlal mass	$4.086 \times 10^{-21}J$	$4.086 \times 10^{-21}J$
N_v^P	Number of vertices	~	-
N_s^P	Number of springs	~	-
μ_0^P	Linear shear modulus	$6.3 \times 10^{-6}J/m^2$	-
Y^P	Young's modulus	$18.9 \times 10^{-6}J/m^2$	-
η^P	Viscosity	$0.022Pa \cdot s$	$0.0013Pa \cdot s$
k_c^P	Bending rigidity	$2.4 \times 10^{-19}J$	-

4.2.2 Physical quantities in model units and parameters of the model

In the mathematical framework-based model, the physical quantities and model parameters, represented in model units, are summarized in Tables 2 and 3. Model units and scaling factors will be discussed in the next section. Since Young's modulus(3D) Y_V^P for the emulsion droplet is much larger than that of the cell, and the volume of the

emulsion droplet is much smaller than that of the cell, the emulsion droplet can be regarded as a rigid sphere passing through the cell gap, and the deformability is mainly reflected in the flexibility of the cell. Therefore, the mesoscale viscoelastic membrane model is still used to represent the cell, and the DPD particle is used to represent the emulsion droplet, and cut-off radius of DPD forces on the DPD particles are set to control the volume of emulsion droplet.

Table 2 Physical Quantities in Model Units

Physical Quantity			Value	
Symbol	Meaning	Notice	Cell	Droplet
L_0^M	Characteristic length		20λ	0.5λ
$(k_BT)^M$	Energy unit per unit particule mass		0.084ξ	0.084ξ
N_c^M	Number of vertices		5206	-
N_s^M	Number of springs		15612	-
μ_0^M	Linear shear modulus	set	$100\xi/\lambda^2$	-
K^M	Elastic area-compression modulus	By Eq.19	$5200\xi/\lambda^2$	-
Y^M	Young's modulus	By Eq.20	$392.45\xi/\lambda^2$	-
ν^M	Poisson's radio	By Eq.21	0.962	-
η^M	Viscosity	By Eq.25	$168.87\nu \cdot \tau$	-
k_c^M	Bending rigidity		5.0165ξ	-

Table 3 Parameters of the Model

Parameters of Models		Value	
Symbol	Notice	Cell	Droplet
r_c	Cut-off distance for DPD particle	1.58λ	0.5λ
l_0	Equilibrium length, In Eq.9	8.58λ	-
x_0	Maximum spring extension ratio, In Eq.9	2.2	-
l_m	Maximum spring extension, In Eq.9, $l_m = x_0 l_0$	18.87λ	-
p	Persistence length, In Eq.9	~	-
k_p	POW force coefficient, In Eq.9	~	-
m	Exponent in POW function, In Eq.9	2.0	-

k_a	Global area constraint constants, In Eq.11	$4900\xi/\lambda^2$	-
k_d	Local area constraint constants, In Eq.11	$100\xi/\lambda^2$	-
k_v	Volume constraint constants, In Eq.12	$5000\xi/\lambda^2$	-
A_0^{tot}	Desired total area, In Eq.11	$6.2\times10^5\lambda^2$	-
A_0	Desired local area, In Eq.11	$31.79\lambda^2$	-
V_0^{tot}	Desired total volume, In Eq.12	$1.5\times10^7\lambda^3$	-
a	DPD conservative force coefficient, In Eq.3	4.0	2.0
γ^C	MVMM dissipative coefficient, In Eq.23	30	-
γ^T	MVMM dissipative coefficient, In Eq.23	90	-
σ^C	MVMM random coefficient, In software	~	-
σ^T	MVMM random coefficient, In software	~	-
γ	DPD dissipative force coefficient, In Eq.4	30	45
σ	DPD random force coefficient, In Eq.5, By Eq.6	2.38	2.76
k_b	Bending coefficient, In Eq.10, By Eq.22	5.79ξ	-
ϕ_0	Spontaneous angle, In Eq.10, By Eq.22	0°	-

L_0^M, N_c^M, N_s^M, A_0^{tot}, V_0^{tot} presented are extracted from the establishment to the model. l_0 and A_0 are mean values obtained from mesh generation statistical results due to the stress-free model. According to equations 9 and 15, k_p and p could be obtained by the μ_0^M formula and equating by attractive and repulsive force formula and be auto calculated in the software without need of input (Fedosov et al., 2010; Tang & Karniadakis, 2014). σ^C and σ^T are auto calculated in the software according to the Eq.6 and $(k_BT)^M$. k_c^M is calculated by k_c^P and energy unit ξ. In the simulations, μ_0^M, k_a, k_d, k_v, γ^T and γ reference to other works (Pozrikidis, 2010; Yazdani et al., 2021).

Table 4 Scaling Factor between Physical Units and Model Units

Symbol	Meaning	Notice	Value
λ	length unit	By Eq.26	$1\times10^{-6}m$
ξ	energy unit	By Eq.27	$4.81586\times10^{-20}J$
ϵ	force unit	By Eq.28	$4.81586\times10^{-14}N$
ν	pressure unit	By Eq.29	$4.81586\times10^{-2}Pa$

τ	time unit	By Eq.30	$2.70518 \times 10^{-3} s$
μ	mass unit	Eq.31	$3.52425 \times 10^{-13} kg$

4.3 Methods of modeling and simulating:

The cell modeling process begins with the use of DistMesh algorithm [74,75] written by MATLAB to draw triangular mesh based on the input shape in terms of distance function without considering the accurate representation of the number of actins and spectrins [54]. Then, a system modeling script is constructed using Python to generate simulation model in the data format that can be read by revised version LAMMPS [60,66] which contains the MVMM model.

Periodic boundary conditions are applied in the simulation box. In addition, Lennard-Jones potential functions are added between the droplet particles and cells to serve as bounce-back boundary conditions to prevent emulsion particle transport into the interior of the cell. Walls are also added at the top and bottom of the z-axis to prevent DPD particles from crossing. The particle representing the Pickering emulsion is distributed at the top free motion zone randomly based on the norm distribution of the average mean velocity and direction vector. An external downward force is applied on the Pickering emulsion to represent the effect of pressure. The cells in the middle of the box are fixed with force to prevent significant displacement due to the effect of the extracellular matrix. At the apical and basal vertices of the cell, additional bonds are introduced to connect with the nearest wall particles, ensuring the stabilization of the cell's position, and reflecting the restrictive role of the extracellular matrix on cell movement.

4.4 Results

4.4.1 Computational efficiency analysis

Based on the method illustrated before, the top view picture of the simulation box is illustrated in Figure 20. The size of the simulation box is $84\lambda \times 84\lambda \times 120\lambda$. The diameter of a muscular cell is 20λ. The length of a muscular cell 70λ, which is shorter than the actual length, to simplify the simulated model. Every cell is uniformly distributed in the middle of the simulation box. In this case, the gap between the cells is set as 1λ. Every muscular cell is constituted of 5206 nodes and 15612 bonds. The total number of cells is 16. As for the particles representing Pickering emulsion, the total number is 141 and they are randomly distributed at the top area of the simulation box satisfying the Gaussian distribution. The average velocity of the Pickering emulsion droplet particle is $0.01082072\lambda/\tau$ and the average direction of initial velocity is [1,0,0], which is perpendicular to the cell axis direction of distribution. The density of distribution is 0.001. As for the particles representing the walls, the number is 14112. They are uniformly distributed in the XY plane at both ends of the Z axis. The total number of particles for the simulation system is 97549. The total number of bonds is 249824. The total number of angles is 166528. The total number of dihedrals is 249792.

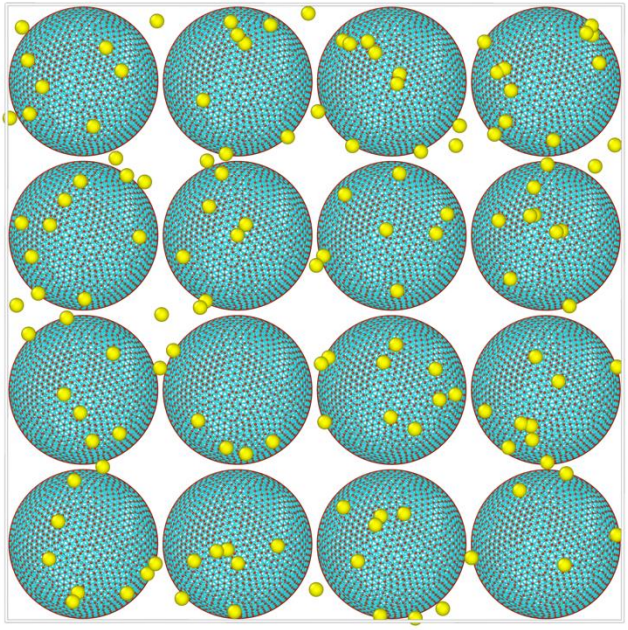

Figure 20 The top view picture of the simulation box

To maximize the proficiency of simulation, the parallel computing ability is tested. The results are shown in Table 5. The version of GPU is Tesla K80 and the result shows that the results show that the GPU parallel capability of the software used is relatively poor. Therefore, all cases use single-card computing. For one computing task whose timesteps is set to 1000000 steps, the time cost is about 81264 seconds. The parallel computing ability is not highly effective, therefore the research adopts 1~4 GPU in most cases to achieve high efficiency.

Table 5 The result of parallel computing ability testing on GPU

GPU Numbers	Timesteps	Time cost	GPU memory cost	GPU efficiency
12	1000	18.3394s	247-252M	29-96%
8	1000	15.156s	263M	85-96%
6	1000	33.1031s	278-288M	32-97%
4	1000	28.277s	315M	92-98%
2	1000	37.1292s	404M	94-99%
1	1000	66.4075s	585M	95%

4.4.2 Criteria for the transport process

To evaluate the efficiency of the transport phenomenon of Pickering emulsion between muscular cells from the microscopic viewpoint method, the criteria is selected as the diffusion coefficient which is obtained by the mean square of displacement (MSD) [62] according the Einstein's theory for Brownian motion and transport time along the fixed distance from the end to end.

The diffusion coefficients (D) were calculated by analyzing the trajectories of particles obtained from dynamics simulations. The positional data for each particle was collected over time to compute the MSD. The MSD for each particle was determined using the formula:

$$\mathrm{MSD}(\Delta t) = \langle [\mathbf{r}(t + \Delta t) - \mathbf{r}(t)]^2 \rangle \tag{32}$$

where $\mathbf{r}(t)$ is the position vector of a particle at time t, and the angle brackets $\langle\rangle$ denote an ensemble average over all particles and a temporal average over multiple starting points to ensure statistical robustness.

The MSD values were plotted against time intervals Δt to ensure a linear relationship, indicating diffusive behavior. A linear regression analysis was performed on the MSD versus Δt plot to extract the slope, which corresponds to $6D$ in three-dimensional systems, following Einstein's relation for diffusion. The diffusion coefficient D was then calculated by dividing the slope by 6:

$$D = \frac{\text{Slope of MSD vs. } \Delta t}{6} \tag{33}$$

All units were corrected to ensure that D was expressed in terms of length^2/time. The following Figure 21 shows the ensembled averaged MSD result of Pickering emulsion which demonstrates a near-linear relationship with the time delta.

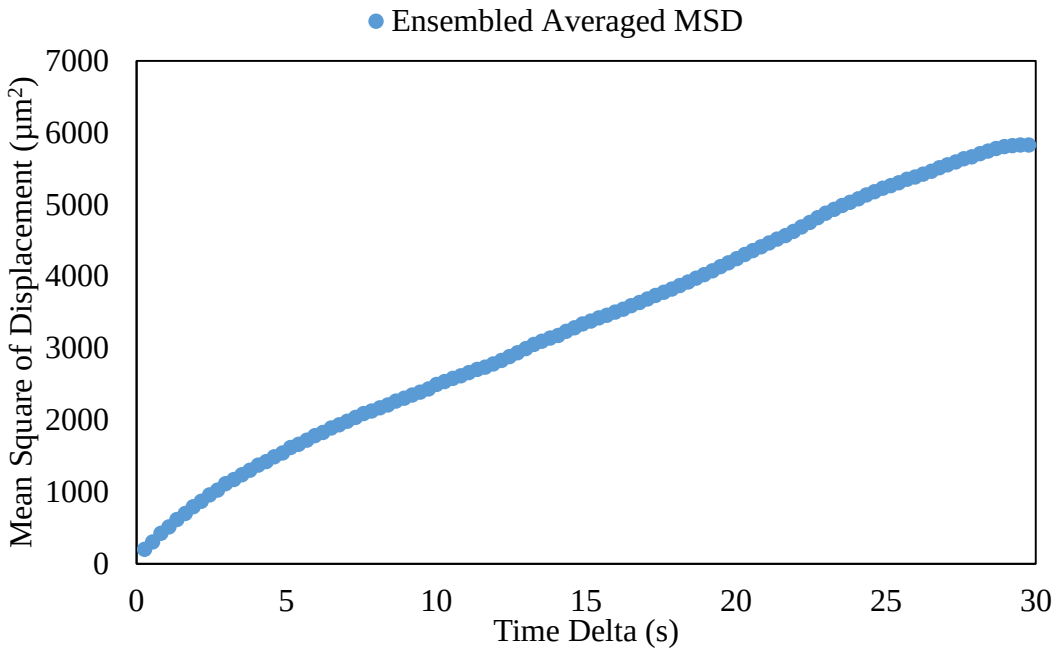

Figure 21 Ensemble Averaged Mean Square of Displacement (MSD)

4.4.3 Quantitative analysis of factors affecting the transport process

We initially examined the conservative force parameter a in DPD, investigating its values at 1.0, 2.0, and 3.0. It can be observed from the Figure 22 that as the conservative force parameter a increases, the diffusion coefficient of the Pickering emulsion decreases, and the diffusion time correspondingly increases. This outcome illustrates the role of parameter a in modulating inter-particle interactions, which in turn affects the diffusion behavior of particles in the emulsion. Given that the conservative force in the DPD method represents the radial repulsive force between a pair of particles, it can indicate that an increase in a leads to enhanced repulsive forces between particles, resulting in greater particle separation and a reduced likelihood of particle movement due to concentration gradients. This enhanced repulsion may cause particles to be more dispersed in space, thereby increasing the difficulty and time required for them to diffuse to a specific region. Moreover, the reduction in diffusion coefficient and the increased transport time may also imply a more stable spatial organization of Pickering emulsion particles. In certain applications, such as drug delivery systems, this increased stability may be beneficial as it can slow down the release of active components.

However, for processes that require rapid diffusion and mixing, such as in catalytic reactions, increased repulsive forces and decreased diffusion coefficients may not be desirable effects. There is a potential link between particle characteristics (such as surface modification or polarity size) and the DPD conservative force parameter. If emulsion particles are modified on their surface to enhance their interactions, this could lead to an increase in repulsion, thereby affecting the diffusion process. This indicates that the design and optimization of emulsions should consider not only the chemical properties of the particles but also their interactions in the simulation environment.

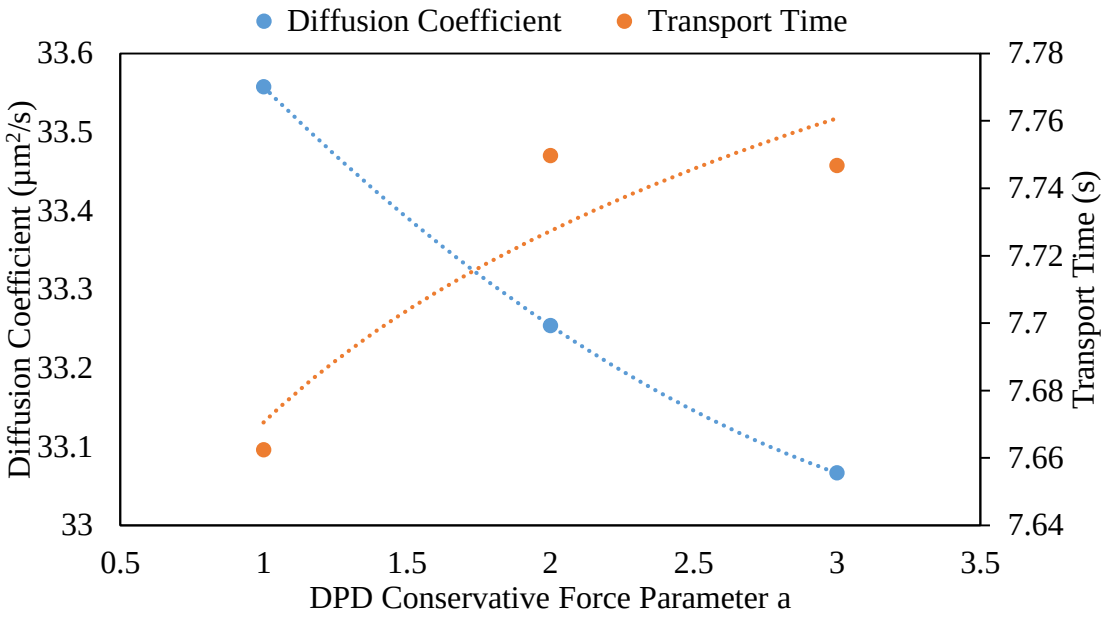

Figure 22 The Influence of DPD Conservative Force Parameter of Pickering Emulsion

Further, the impact of local cellular tissue environmental factors on the transport efficiency of Pickering emulsion is investigated, as shown in Figures 23-25. The driving force applied to the Pickering emulsion can be approximated as the pressure in the local tissue cellular environment or the external driving force from the muscle injection process or the driving force from concentration differences. Under these driving forces, Figure 23 indicates that the Pickering emulsion droplets would traverse through the

intercellular gaps within the tissue faster under greater local driving forces. The increased diffusion coefficient with higher applied force suggests that the droplets are experiencing less resistance in the medium, allowing them to spread more quickly. This could be due to the fact that higher forces help to overcome the various frictional and viscous forces that act on the droplets, facilitating their movement through the tissue matrix. Conversely, the decrease in transport time with increased force implies that the droplets can reach their target sites more rapidly. This is particularly relevant in medical applications where the time-sensitive delivery of therapeutic agents is crucial. The ability to control the transport time of the emulsion droplets by adjusting the applied force could lead to more efficient and targeted drug delivery strategies. By fine-tuning the applied force, it may be possible to enhance the penetration of droplets through the intercellular gaps of tissues, ensuring that the active agents are distributed evenly and reach the site of action effectively. Moreover, the relationship between force and transport properties could be further exploited to understand the interaction of droplets with complex tissue structures. For example, in dense or fibrous tissues, higher forces might be required to achieve the same level of diffusion as in less dense tissues. Understanding these relationships can aid in the design of emulsion-based delivery systems that are customized for specific tissue types and therapeutic needs.

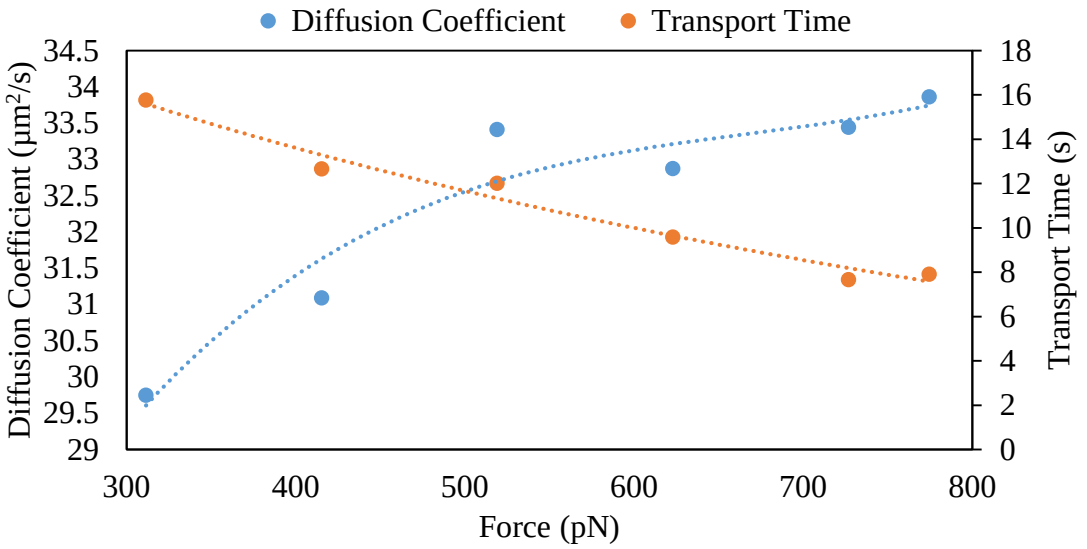

Figure 23 The Influence of Pushing Force on Pickering Emulsion

Concurrently, the influence of the statistic average initial velocity vector direction of the Pickering emulsion on its transport efficiency was examined. Figure 24 presents the impact of the initial velocity vector direction of Pickering emulsion droplets on their transport efficiency. The direction vector (1,0,0) represents a direction perpendicular to the axial alignment of the cells, whereas the direction vector (0,0,-1) represents a direction parallel to the axial alignment of the cells. It is observable that the transport efficiency is higher when the average direction vector of the velocity is closer to the axial alignment direction of the cells. Intuitively, when the movement direction of droplets is aligned with the principal axis of the cells, their path through the intercellular gaps is more direct, which may reduce the resistance they encounter during motion, thereby enhancing transport efficiency. These findings emphasize the importance of considering not only the chemical and physical properties of emulsion droplets in the design of emulsion-based drug delivery systems but also their kinematic characteristics, including the direction of the direction of the velocity vector. By adjusting the initial direction of velocity during the injection or delivery process, the delivery path and timing of therapeutic agents can be optimized.

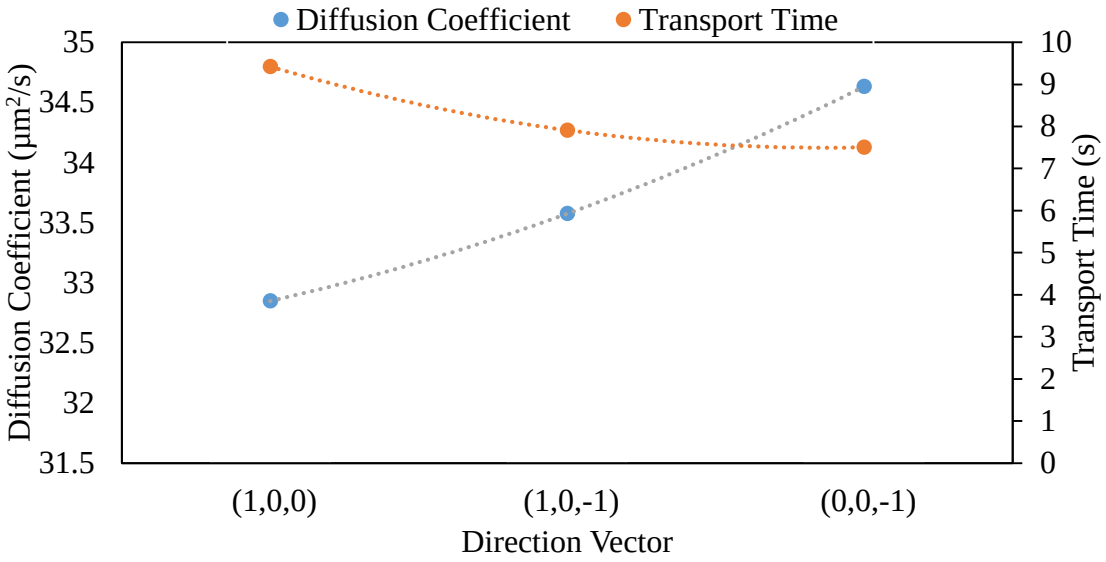

Figure 24 The Influence of the Direction Vector of Pickering Emulsion

Moreover, in the modeling, the size of the intercellular gaps between cells is altered to inspect the influence of the cellular environment within the tissue on the Pickering emulsion. Figure 25 denotes that larger intercellular gaps actually lower the diffusion coefficient, while the transport time of the Pickering emulsion consequently increases. The results shown in Figure 7 might seem counterintuitive to initial assumptions, which could be attributed to the following reasons: Here, the Pickering emulsion droplets have an average initial velocity direction that is perpendicular to the axial alignment of the cells. Therefore, lateral diffusion contributes significantly to the diffusion process, and the increase in intercellular gaps markedly lengthens the path for lateral diffusion. This increases the likelihood of encountering obstacles or taking more circuitous paths, as the droplets are more influenced by interactions with the spaces between cells, with an increased chance of collisions, thereby enhancing the complexity of the path during diffusion. This complexity leads to a significant increase in energy dissipation throughout the diffusion process, thereby reducing the droplets' kinetic energy, resulting in a decreased diffusion coefficient and increased transport time. Typically, studies on near-wall hindered diffusion focus on a single channel, whereas the transport phenomena examined here within the tissue present a complexity that goes far beyond

a single channel, specifically, for Pickering emulsion droplets, the contributions resulting from longer lateral diffusion distances, more complex diffusion pathways, and more frequent interactions with the walls of the diffusion channels outweigh the contributions from single near-wall hindered events [82], thus exhibiting the characteristics seen in Figure 25.

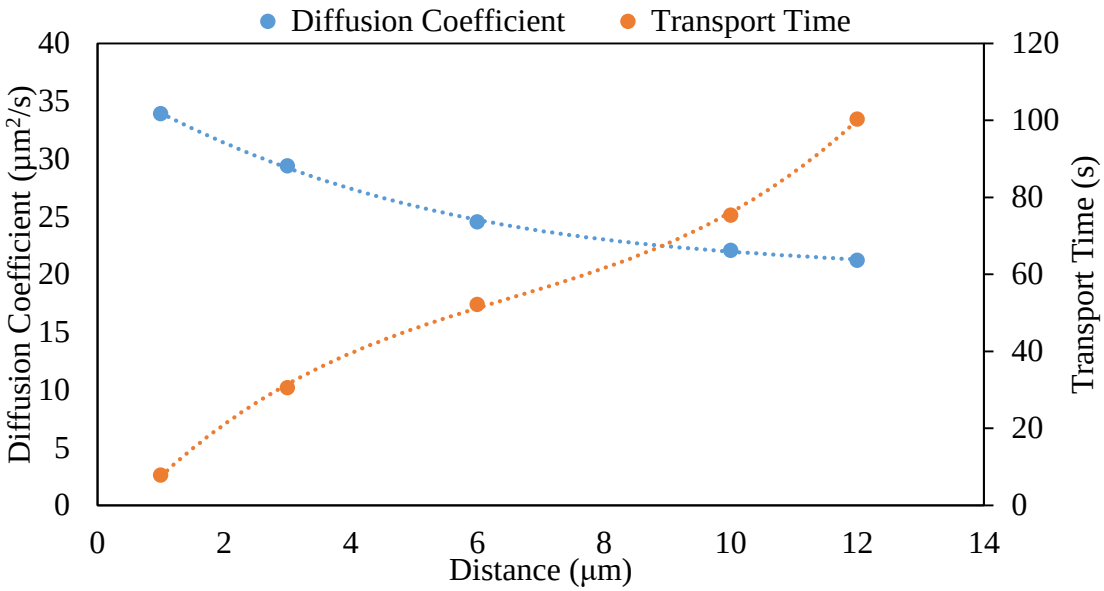

Figure 25 The Influence of Size of Gaps between Cells

Further investigations are conducted on other factors affecting the transport performance of Pickering emulsion, including viscosity (represented by the DPD dissipative force parameter gamma), temperature, interaction between Pickering emulsion and cell (represented by DPD conservative force parameter between DPD particle and cell model), and the initial velocity magnitude of Pickering emulsion. Considering the fluctuation-dissipation theorem and the fact that the shear modulus of cells changes with variations in environmental temperature, Table 6 summarizes the impact of temperature variations on various parameters within the model. Table 7 summarizes the variance values of the diffusion coefficient under the influence of various parameters, indicating that the variance of the $\gamma_{particle}$ parameter of DPD

emulsion droplets is the smallest, implying that surface viscosity has a relatively smaller impact on the transport of Pickering emulsion compared to the other parameters listed here.

Table 6 Analyses for Parameters of Temperature

T	$(k_BT)^M$	$(k_BT)^M$	$\sigma_{Particle}$	σ_{cell}	μ_0^P	μ_0^M
296K	$4.086 \times 10^{-21}J$	0.0848	2.763	2.256	$6.30 \times 10^{-6}N/m$	100.00
303K	$4.183 \times 10^{-21}J$	0.0868	2.796	2.282	$6.16 \times 10^{-6}N/m$	97.73
308K	$4.252 \times 10^{-21}J$	0.0882	2.819	2.301	$6.12 \times 10^{-6}N/m$	97.20
310K	$4.280 \times 10^{-21}J$	0.0888	2.828	2.309	$5.80 \times 10^{-6}N/m$	92.06
312K	$4.307 \times 10^{-21}J$	0.0894	2.837	2.316	$5.39 \times 10^{-6}N/m$	85.60
314K	$4.335 \times 10^{-21}J$	0.0900	2.846	2.324	$4.90 \times 10^{-6}N/m$	77.78

Table 7 Analysis of Variance of Simulation Parameters

Parameter	Range	Mean Value	Variance
$\gamma_{particle}$	25~45	0.085007429	1.89194×10^{-6}
a_{inter}	1~5	0.088832662	5.66877×10^{-6}
T	$296\sim314K$	0.090481135	8.93948×10^{-6}
$velocity$	$4\sim15\mu m/s$	0.092851366	7.54986×10^{-6}

Notice that this study didn't consider the adhesion influence between cells and emulsion particles, which could further decrease the transport efficiency of Pickering emulsion droplets between tissues and affect the distribution of Pickering emulsion in a real muscular tissue environment. Besides, in order to reflect the pressure within the tissue, this simulation is during an unsteady process. The current model only incorporates the effects of radial repulsive conservative forces; some research work [83–86] considering DPD particles with fixed charge may suggest the potential to include the effects of charge forces in the model. As for the influence of viscosity, this study doesn't show the apparent correlation on the $\gamma_{particle}$ parameter, which could be concluded from the thermostat setting is not enough, which is the Langevin thermostat

in this study, maintaining the temperature by modifying Newton's equations of motion [87].

4.5 Summary

Based on the elaborated results and discussions, the following conclusions can be drawn regarding the transport phenomenon of Pickering emulsion between muscular cells:

a. The transport efficiency of Pickering emulsion is significantly influenced by a variety of factors including the conservative force parameter in the DPD method, local cellular tissue environmental factors, viscosity, temperature, interaction between Pickering emulsion and cell, and the initial velocity magnitude of Pickering emulsion.

b. The impact of the local cellular environment within the tissue significantly affects the transport efficiency of Pickering emulsion. Specifically, greater local driving forces, which could be due to the pressure in the local tissue cellular environment or external driving forces from muscle injection process or concentration differences, expedite the traversal of Pickering emulsion droplets through the intercellular gaps within the tissue. Moreover, the orientation of the initial velocity vector of the Pickering emulsion towards the axial direction of the cells enhances the transport efficiency. Conversely, an increase in the size of the intercellular gaps leads to a decrease in the diffusion coefficient and an increase in the transport time of the Pickering emulsion.

c. An increase in the conservative force parameter a in the DPD method, representing the radial repulsive force between particles, leads to a decrease of the diffusion coefficient and a corresponding increase of diffusion time for Pickering emulsion. This suggests that a larger mutual repulsive force among Pickering emulsion

particles potentially results in lower transport efficiency. The magnitude of this repulsive force could be attributed to factors such as the surface modification or polarity size of the Pickering emulsion. Among other investigated factors, the variance of the gamma parameter of DPD emulsion droplets is found to be the smallest, suggesting that surface viscosity has a relatively lesser impact on the transport of Pickering emulsion.

These findings provide a comprehensive understanding of the various factors affecting the transport efficiency of Pickering emulsion between muscular cells, which is crucial for optimizing the transport process in practical applications. The insights gained from this study could be instrumental in designing more effective transport systems for Pickering emulsion, thereby facilitating its potential applications in drug delivery and other relevant fields.

The study highlights key design principles for biocompatible Pickering emulsions used as drug delivery systems by exploring the effects of various factors on their transport efficiency. Increasing the conservative force parameter 'a' in DPD simulations decreases diffusion coefficients and increases diffusion time, indicating a stronger repulsive force and greater particle separation. This could enhance the stability of the emulsion, beneficial in applications like slow-release drug delivery systems. Local driving forces, such as pressure and forces from muscle injections, can speed up the transport of emulsion droplets through tissue intercellular gaps, suggesting that external force application could be fine-tuned for more effective and targeted drug delivery. Furthermore, the orientation of the initial velocity vector of the emulsion affects transport efficiency, with alignment parallel to the axial alignment of cells being more efficient. The size of intercellular gaps has a complex influence on transport, with larger gaps potentially increasing transport time due to more complex diffusion paths and energy dissipation. Other factors like viscosity, temperature, emulsion-cell interactions, and the initial velocity magnitude of the emulsion also affect transport performance.

Additionally, based on the analysis of the physiological structure of lymphatic capillaries and collecting vessels, the 2-micron-wide pillow structures on capillary lymphatics, which open and close under interstitial to intraluminal pressure gradients, may provide a pathway for fluid transport for the transportation of Pickering emulsion. This mechanism potentially facilitates the movement of Pickering emulsion within the lymphatic system, thereby broadening the understanding of how the physiological architecture can influence the transport dynamics of Pickering emulsion. This aspect exemplifies the interdependence between biological structures and the transport phenomena of nano or micro-scale emulsions like Pickering emulsion, enriching the comprehension of how engineering and biological systems can be integrated for enhanced performance in biomedical applications.

Chapter 5 Conclusions and Perspectives

5.1 Conclusion

Pickering emulsion has become an advantageous material for vaccine adjuvants in recent years because of its good stability, high controllability, and excellent biocompatibility, especially the vaccine adjuvant prepared with Pickering emulsion in Xia et al.'s experiment owned the advantage of high efficiency of immune response, and they developed a deformable albumin-stabilized Pickering emulsion according to the dual LN transfer strategy combining the intracellular pathway and intercellular pathway, which clearly augments antigen build-up and activates lymph node drainage, thereby efficiently boosting cellular immune reactions. However, comprehensive studies elucidating the intracorporeal delivery mechanisms of Pickering emulsions, especially the intricate intercellular interactions of deformable Pickering emulsions, remain significantly scarce and have historically received minimal attention. The current understanding of the drug delivery process, particularly quantitative analysis and simulated models is still quite limited. Most knowledge of this process, especially for soft and deformable droplets like Pickering emulsions, remains vague. At present, the depth of understanding and simulation of internal kinematics at the tissue level within the human body is profoundly limited, and there is a significant lack of effective models. To clarify this mechanism and facilitate the future development of this material, in this research, the intrinsic mechanism for the key process from perspective of tissue level was analyzed in detail by employing computational simulation techniques.

First, the thesis elucidates the delivery process of Pickering emulsion through intracellular and intercellular pathways at the tissue level, according to the physiological characteristics of tissues and cells related to the transport process of Pickering emulsion. The total process could be divided into the following steps

separately in sequence: muscular injection, transport in skeletal muscle tissue, flow through gaps between flaps of lymphatic endothelial cells of lymph capillary, flow through lymph vaccine, and accumulation in the lymph node. For the intracellular pathway, Antigen-presenting cells, such as dendritic cells, undergo the process of antigen uptake within skeletal muscle tissue, where the antigen carrier during delivery is the dendritic cell itself. For the intercellular pathway, dendritic cells undergo the process of antigen uptake within the lymph nodes, and the antigen carrier during delivery in this scenario is the Pickering emulsion. The opening and closing mechanism of the flap of lymph endothelial cells of lymphatic capillaries under the influence of internal and external pressure provides a fluid way for the transport of flexible particles.

Secondly, to depict the internal kinematics at the tissue level within the human body, this thesis enhanced a more advanced model at the mesoscale according to the dissipative particle dynamics simulation method. By organizing and clarifying the relationships between concepts, the scaling factor was derived, further elucidating its relationship to coarse-graining, and this understanding was extended to a variety of cell types. The DPD simulation framework represents a significant advance in the modeling of natural systems, especially in the field of drug delivery. It stands as a robust approach to understanding the complex interactions within cellular environments, paving the way for future innovations in the simulation and analysis of biological systems.

Thirdly, according to features of the cellular model under the DPD simulation framework, this thesis successfully applied the DistMesh algorithm to generate the different shape cells to depict its cytoskeletal. The mesh results indicate that the distribution of nodes exhibits a commendable level of uniformity. The comparatively symmetrical triangles align well with the requirements for a two-dimensional tetrameric lattice of the cytoskeleton, suggesting suitability for representing the cellular framework. Besides based on this model, the stretching test of red blood cell shows a

good mechanical response consistent with the experiment. It paves the way for future investigations into the mechanical properties of cells and the role of the cytoskeleton. It provides robust tool and theory support for further observations of biological activity from the perspective of cellular organization.

Fourthly, the research first investigates the Pickering emulsion transport in the skeletal muscle tissue to clarify the intercellular pathway mechanism and examine various factors affecting the transport process. The transport efficiency of Pickering emulsions is significantly influenced by a range of factors. The conservative force parameter in the DPD method affects the repulsion between particles, impacting the diffusion coefficient and transport time. Local cellular tissue environmental factors, including local driving forces such as pressure and external forces from processes like muscle injection or concentration gradients, facilitate the movement of Pickering emulsion droplets through tissue gaps. Additionally, factors such as viscosity, temperature, emulsion-cell interactions, and the initial velocity of the emulsion all play roles in transport efficiency. The initial velocity's directionality towards the cell axial direction also enhances efficiency, while larger intercellular gaps can reduce it. Interestingly, the surface viscosity, as indicated by the gamma parameter variance in DPD emulsion droplets, appears to have a lesser impact compared to other factors like surface modification or polarity size of the emulsion, which affect the magnitude of the repulsive force among the emulsion particles.

This study sheds light on the nuanced interplay between engineered and biological systems influencing the transport dynamics of Pickering emulsions. Such insights hold valuable potential for optimizing transport processes in practical biomedical applications like drug delivery. Importantly, the desired transport efficiency varies depending on the specific application. For instance, while a more rapid transport might be crucial for lymph node-targeted drug delivery, certain applications requiring a

slower release of active components could benefit from the reduced transport efficiency observed with increased particle repulsion or larger intercellular gaps.

5.2 Perspectives

Pickering emulsions are emerging as potent vehicles for vaccine adjuvants, prized for their stability, tunability, and biocompatibility. The work by Xia et al. highlights a novel albumin-stabilized Pickering emulsion designed for dual lymph node (LN) transfer pathways—both intracellular and intercellular. This dual-pathway approach maximizes antigen delivery, enhancing LN accumulation and activation, thereby stimulating a robust cellular immune response. Despite the advantages, a comprehensive understanding of Pickering emulsion transport mechanisms within the body, particularly the complex intercellular interactions, remains underexplored. The current landscape of quantitative analysis and simulated models for drug delivery is nascent, with the transport processes, especially of malleable droplets like Pickering emulsions, remaining largely uncharted.

Crucially, this research methodically examines the transport of Pickering emulsions in skeletal muscle tissue, establishing a more intricate understanding of the intercellular pathway and identifying multiple influencing factors. It reveals how local cellular tissue environments, viscosity, temperature, and other variables can affect the efficiency of Pickering emulsion transport. The findings point to the potential for further explorations into the mechanical behaviors of cells and the intricacies of biological activity at a cellular level.

In advancing the cellular model that incorporates particles, future efforts will focus on achieving more precise modeling by incorporating the effects of angular momentum, considering the impact of solvent particles, and coupling with the Grand Canonical

Monte Carlo (GCMC) method. Additionally, the influence of boundary conditions will be meticulously considered. This includes a more accurate calculation of the Cauchy stress, leveraging a modern and precise expression of virial stress. Regarding the investigation of vaccine delivery via the intercellular pathway, further simulations are necessary to understand the valves' opening and closing mechanism in lymphatic endothelial cells (LECs) of capillary lymphatic vessels, especially under varying pressure conditions influenced by Pickering emulsions. Moreover, simulating lymphatic flow within lymphatic vessels in the presence of Pickering emulsions will provide deeper insights into the complex dynamics of vaccine distribution and the resulting immunological responses. These enhancements in modeling and simulation are pivotal in refining our understanding of vaccine delivery mechanisms, ultimately leading to the development of more efficient and targeted vaccine administration strategies.

In summary, this study not only advances our theoretical and practical knowledge of Pickering emulsions as vaccine adjuvants but also sets the stage for future breakthroughs in the simulation and analysis of biological transport systems, contributing to the development of more effective biomedical materials.

Reference

[1] M. Li, H. Wang, L. Tian, Z. Pang, Q. Yang, T. Huang, J. Fan, L. Song, Y. Tong, H. Fan, COVID-19 vaccine development: milestones, lessons and prospects, Signal Transduct. Target. Ther. 7 (2022) 146. https://doi.org/10.1038/s41392-022-00996-y.

[2] S. Su, L. Du, S. Jiang, Learning from the past: development of safe and effective COVID-19 vaccines, Nat. Rev. Microbiol. 19 (2021) 211–219. https://doi.org/10.1038/s41579-020-00462-y.

[3] A. Schudel, D.M. Francis, S.N. Thomas, Material design for lymph node drug delivery, Nat. Rev. Mater. 4 (2019) 415–428. https://doi.org/10.1038/s41578-019-0110-7.

[4] T. Song, Y. Xia, Y. Du, M.W. Chen, H. Qing, G. Ma, Engineering the Deformability of Albumin-Stabilized Emulsions for Lymph-Node Vaccine Delivery, Adv. Mater. 33 (2021) 2100106. https://doi.org/10.1002/adma.202100106.

[5] A.J. Najibi, D.J. Mooney, Cell and tissue engineering in lymph nodes for cancer immunotherapy, Adv. Drug Deliv. Rev. 161–162 (2020) 42–62. https://doi.org/10.1016/j.addr.2020.07.023.

[6] Y. Ding, Z. Li, A. Jaklenec, Q. Hu, Vaccine delivery systems toward lymph nodes, Adv. Drug Deliv. Rev. 179 (2021) 113914. https://doi.org/10.1016/j.addr.2021.113914.

[7] A.M. Sousa, M.J. Pereira, H.A. Matos, Oil-in-water and water-in-oil emulsions formation and demulsification, J. Pet. Sci. Eng. 210 (2022) 110041. https://doi.org/10.1016/j.petrol.2021.110041.

[8] T.F. Tadros, Emulsions: Formation, Stability, Industrial Applications, De Gruyter, 2016. https://doi.org/10.1515/9783110452242.

[9] M. E. Mohyaldinn, A. M. Hassan, M. A. Ayoub, Application of Emulsions and Microemulsions in Enhanced Oil Recovery and Well Stimulation, in: Microemulsion - Chem. Nanoreactor Work. Title, IntechOpen, 2019. https://doi.org/10.5772/intechopen.84538.

[10] Y. Yang, Z. Fang, X. Chen, W. Zhang, Y. Xie, Y. Chen, Z. Liu, W. Yuan, An Overview of Pickering Emulsions: Solid-Particle Materials, Classification, Morphology, and Applications, Front. Pharmacol. 8 (2017) 287. https://doi.org/10.3389/fphar.2017.00287.

[11] F.B. De Carvalho-Guimarães, K.L. Correa, T.P. De Souza, J.R. Rodríguez Amado, R.M. Ribeiro-Costa, J.O.C. Silva-Júnior, A Review of Pickering Emulsions: Perspectives and Applications, Pharmaceuticals 15 (2022) 1413. https://doi.org/10.3390/ph15111413.

[12] Z. Sun, X. Yan, Y. Xiao, L. Hu, M. Eggersdorfer, D. Chen, Z. Yang, D.A. Weitz, Pickering emulsions stabilized by colloidal surfactants: Role of solid particles, Particuology 64 (2022) 153–163. https://doi.org/10.1016/j.partic.2021.06.004.

[13] J. Pan, J. Chen, X. Wang, Y. Wang, J. Fan, Pickering emulsion: From controllable fabrication to biomedical application, Interdiscip. Med. 1 (2023) e20230014. https://doi.org/10.1002/INMD.20230014.

[14] Y. Xia, J. Wu, W. Wei, Y. Du, T. Wan, X. Ma, W. An, A. Guo, C. Miao, H. Yue, S. Li, X. Cao, Z. Su, G. Ma, Exploiting the pliability and lateral mobility of Pickering emulsion for enhanced vaccination, Nat. Mater. 17 (2018) 187–194. https://doi.org/10.1038/nmat5057.

[15] Y. Ming, Y. Xia, G. Ma, Aggregating particles on the O/W interface: Tuning Pickering emulsion for the enhanced drug delivery systems, Aggregate 3 (2022) e162. https://doi.org/10.1002/agt2.162.

[16] P. Baluk, J. Fuxe, H. Hashizume, T. Romano, E. Lashnits, S. Butz, D. Vestweber, M. Corada, C. Molendini, E. Dejana, D.M. McDonald, Functionally

specialized junctions between endothelial cells of lymphatic vessels, J. Exp. Med. 204 (2007) 2349–2362. https://doi.org/10.1084/jem.20062596.

[17] J.W. Breslin, Mechanical forces and lymphatic transport, Microvasc. Res. 96 (2014) 46–54. https://doi.org/10.1016/j.mvr.2014.07.013.

[18] A.R. Gillies, R.L. Lieber, Structure and function of the skeletal muscle extracellular matrix, Muscle Nerve 44 (2011) 318–331. https://doi.org/10.1002/mus.22094.

[19] S. Jalkanen, M. Salmi, Lymphatic endothelial cells of the lymph node, Nat. Rev. Immunol. 20 (2020) 566–578. https://doi.org/10.1038/s41577-020-0281-x.

[20] K.N. Margaris, R.A. Black, Modelling the lymphatic system: challenges and opportunities, J. R. Soc. Interface 9 (2012) 601–612. https://doi.org/10.1098/rsif.2011.0751.

[21] J.P. Nederveen, M.W. Betz, T. Snijders, G. Parise, The Importance of Muscle Capillarization for Optimizing Satellite Cell Plasticity, Exerc. Sport Sci. Rev. 49 (2021) 284–290. https://doi.org/10.1249/JES.0000000000000270.

[22] L.H. Nicoll, A. Hesby, Intramuscular injection: An integrative research review and guideline for evidence-based practice, Appl. Nurs. Res. 15 (2002) 149–162. https://doi.org/10.1053/apnr.2002.34142.

[23] O. Ohtani, Y. Ohtani, C.J. Carati, B.J. Gannon, Fluid and cellular pathways of rat lymph nodes in relation to lymphatic labyrinths and Aquaporin-1 expression, Arch. Histol. Cytol. 66 (2003) 261–272. https://doi.org/10.1679/aohc.66.261.

[24] F. Zhang, G. Zarkada, S. Yi, A. Eichmann, Lymphatic Endothelial Cell Junctions: Molecular Regulation in Physiology and Diseases, Front. Physiol. 11 (2020) 509. https://doi.org/10.3389/fphys.2020.00509.

[25] E. Mendoza, G.W. Schmid-Schönbein, A model for mechanics of primary lymphatic valves, J. Biomech. Eng. 125 (2003) 407–414. https://doi.org/10.1115/1.1568128.

[26] L. Meng, Tailoring Conducting Polymer Interface for Sensing and Biosensing, Linköping University Electronic Press, Linköping, 2020.

[27] Preface - Anatomy & Physiology, in: OpenStax, OpenStax CNX, 2016.

[28] K. Xu, G. Zhong, X. Zhuang, Actin, Spectrin, and Associated Proteins Form a Periodic Cytoskeletal Structure in Axons, Science 339 (2013) 452–456. https://doi.org/10.1126/science.1232251.

[29] W.R. Frontera, J. Ochala, Skeletal Muscle: A Brief Review of Structure and Function, Calcif. Tissue Int. 96 (2015) 183–195. https://doi.org/10.1007/s00223-014-9915-y.

[30] D. Zhou, J.A. Ursitti, R.J. Bloch, Developmental Expression of Spectrins in Rat Skeletal Muscle, Mol. Biol. Cell 9 (1998) 47–61. https://doi.org/10.1091/mbc.9.1.47.

[31] J. Banchereau, F. Briere, C. Caux, J. Davoust, S. Lebecque, Y.-J. Liu, B. Pulendran, K. Palucka, Immunobiology of Dendritic Cells, Annu. Rev. Immunol. 18 (2000) 767–811. https://doi.org/10.1146/annurev.immunol.18.1.767.

[32] N. Gong, Y. Zhang, Z. Zhang, X. Li, X. Liang, Functional Nanomaterials Optimized to Circumvent Tumor Immunological Tolerance, Adv. Funct. Mater. 29 (2019) 1806087. https://doi.org/10.1002/adfm.201806087.

[33] D.A. Fedosov, Multiscale Modeling of Blood Flow and Soft Matter, 2010.

[34] N. Liu, M. Becton, L. Zhang, X. Wang, Mechanism of Coupling Nanoparticle Stiffness with Shape for Endocytosis: From Rodlike Penetration to Wormlike Wriggling, J. Phys. Chem. B 124 (2020) 11145–11156. https://doi.org/10.1021/acs.jpcb.0c08089.

[35] W. Pan, A.M. Tartakovsky, Dissipative particle dynamics model for colloid transport in porous media, Adv. Water Resour. 58 (2013) 41–48. https://doi.org/10.1016/j.advwatres.2013.04.004.

[36] L. Zhou, S. Feng, H. Liu, J. Chang, Dissipative particle dynamics simulation of cell entry into a micro-channel, Eng. Anal. Bound. Elem. 107 (2019) 47–52. https://doi.org/10.1016/j.enganabound.2019.07.004.

[37] S. Yip, M.P. Short, Multiscale materials modelling at the mesoscale, Nat. Mater. 12 (2013) 774–777. https://doi.org/10.1038/nmat3746.

[38] E. Engel, R.M. Dreizler, Density functional theory: an advanced course, Springer, Heidelberg [Germany] New York, 2011.

[39] M. Karplus, G.A. Petsko, Molecular dynamics simulations in biology, Nature 347 (1990) 631–639. https://doi.org/10.1038/347631a0.

[40] P. Constantin, C. Foiaş, Navier-Stokes equations, Nachdr., Univ. of Chicago Pr, Chicago, 1989.

[41] T.J. Chung, Computational fluid dynamics, Reprint, Cambridge Univ. Press, Cambridge, 2008.

[42] J.P. Boon, D. Dab, R. Kapral, A. Lawniczak, Lattice gas automata for reactive systems, Phys. Rep. 273 (1996) 55–147. https://doi.org/10.1016/0370-1573(95)00080-1.

[43] P.J. Hoogerbrugge, J.M.V.A. Koelman, Simulating Microscopic Hydrodynamic Phenomena with Dissipative Particle Dynamics, Europhys. Lett. EPL 19 (1992) 155–160. https://doi.org/10.1209/0295-5075/19/3/001.

[44] J.M.V.A. Koelman, P.J. Hoogerbrugge, Dynamic Simulations of Hard-Sphere Suspensions Under Steady Shear, Europhys. Lett. EPL 21 (1993) 363–368. https://doi.org/10.1209/0295-5075/21/3/018.

[45] X. Fan, N. Phan-Thien, S. Chen, X. Wu, T. Yong Ng, Simulating flow of DNA suspension using dissipative particle dynamics, Phys. Fluids 18 (2006) 063102. https://doi.org/10.1063/1.2206595.

[46] D.A. Fedosov, G. Em Karniadakis, B. Caswell, Dissipative particle dynamics simulation of depletion layer and polymer migration in micro- and nanochannels

for dilute polymer solutions, J. Chem. Phys. 128 (2008) 144903. https://doi.org/10.1063/1.2897761.

[47] P. Español, P. Warren, Statistical Mechanics of Dissipative Particle Dynamics, Europhys. Lett. EPL 30 (1995) 191–196. https://doi.org/10.1209/0295-5075/30/4/001.

[48] P. Español, Fluid particle model, Phys. Rev. E 57 (1998) 2930–2948. https://doi.org/10.1103/PhysRevE.57.2930.

[49] W. Pan, D.A. Fedosov, G.E. Karniadakis, B. Caswell, Hydrodynamic interactions for single dissipative-particle-dynamics particles and their clusters and filaments, Phys. Rev. E 78 (2008) 046706. https://doi.org/10.1103/PhysRevE.78.046706.

[50] W. Pan, I.V. Pivkin, G.E. Karniadakis, Single-particle hydrodynamics in DPD: A new formulation, EPL Europhys. Lett. 84 (2008) 10012. https://doi.org/10.1209/0295-5075/84/10012.

[51] E.E. Keaveny, I.V. Pivkin, M. Maxey, G. Em Karniadakis, A comparative study between dissipative particle dynamics and molecular dynamics for simple- and complex-geometry flows, J. Chem. Phys. 123 (2005) 104107. https://doi.org/10.1063/1.2018635.

[52] D.E. Discher, D.H. Boal, S.K. Boey, Simulations of the Erythrocyte Cytoskeleton at Large Deformation. II. Micropipette Aspiration, Biophys. J. 75 (1998) 1584–1597. https://doi.org/10.1016/S0006-3495(98)74076-7.

[53] J. Li, M. Dao, C.T. Lim, S. Suresh, Spectrin-Level Modeling of the Cytoskeleton and Optical Tweezers Stretching of the Erythrocyte, Biophys. J. 88 (2005) 3707–3719. https://doi.org/10.1529/biophysj.104.047332.

[54] I.V. Pivkin, G.E. Karniadakis, Accurate Coarse-Grained Modeling of Red Blood Cells, Phys. Rev. Lett. 101 (2008) 118105. https://doi.org/10.1103/PhysRevLett.101.118105.

[55] D.A. Fedosov, B. Caswell, G.E. Karniadakis, A Multiscale Red Blood Cell Model with Accurate Mechanics, Rheology, and Dynamics, Biophys. J. 98 (2010) 2215–2225. https://doi.org/10.1016/j.bpj.2010.02.002.

[56] D.A. Fedosov, G. Gompper, White blood cell margination in microcirculation, Soft Matter 10 (2014) 2961–2970. https://doi.org/10.1039/C3SM52860J.

[57] A. Yazdani, Y. Deng, H. Li, E. Javadi, Z. Li, S. Jamali, C. Lin, J.D. Humphrey, C.S. Mantzoros, G. Em Karniadakis, Integrating blood cell mechanics, platelet adhesive dynamics and coagulation cascade for modelling thrombus formation in normal and diabetic blood, J. R. Soc. Interface 18 (2021) rsif.2020.0834, 20200834. https://doi.org/10.1098/rsif.2020.0834.

[58] M. Razizadeh, M. Nikfar, R. Paul, Y. Liu, Coarse-Grained Modeling of Pore Dynamics on the Red Blood Cell Membrane under Large Deformations, Biophys. J. 119 (2020) 471–482. https://doi.org/10.1016/j.bpj.2020.06.016.

[59] X. Shi, G. Lin, J. Zou, D.A. Fedosov, A lattice Boltzmann fictitious domain method for modeling red blood cell deformation and multiple-cell hydrodynamic interactions in flow, Int. J. Numer. Methods Fluids 72 (2013) 895–911. https://doi.org/10.1002/fld.3764.

[60] A.L. Blumers, Y.-H. Tang, Z. Li, X. Li, G.E. Karniadakis, GPU-accelerated Red Blood Cells Simulations with Transport Dissipative Particle Dynamics, Comput. Phys. Commun. 217 (2017) 171–179. https://doi.org/10.1016/j.cpc.2017.03.016.

[61] C. Pozrikidis, ed., Computational hydrodynamics of capsules and biological cells, CRC Press, Boca Raton, 2010.

[62] M.P. Allen, D.J. Tildesley, Computer simulation of liquids, Second edition, Oxford University Press, Oxford, United Kingdom, 2017.

[63] M. Dao, J. Li, S. Suresh, Molecularly based analysis of deformation of spectrin network and human erythrocyte, Mater. Sci. Eng. C 26 (2006) 1232–1244. https://doi.org/10.1016/j.msec.2005.08.020.

[64] B. Liu, X. Qiu, How to compute the atomic stress objectively?, (2008). http://arxiv.org/abs/0810.0803 (accessed October 29, 2023).

[65] L. Zhang, J. Jasa, G. Gazonas, A. Jérusalem, M. Negahban, Extracting continuum-like deformation and stress from molecular dynamics simulations, Comput. Methods Appl. Mech. Eng. 283 (2015) 1010–1031. https://doi.org/10.1016/j.cma.2014.10.018.

[66] Y.-H. Tang, G.E. Karniadakis, Accelerating Dissipative Particle Dynamics Simulations on GPUs: Algorithms, Numerics and Applications, Comput. Phys. Commun. 185 (2014) 2809–2822. https://doi.org/10.1016/j.cpc.2014.06.015.

[67] P. Español, Dissipative particle dynamics with energy conservation, Europhys. Lett. EPL 40 (1997) 631–636. https://doi.org/10.1209/epl/i1997-00515-8.

[68] Z. Li, A. Yazdani, A. Tartakovsky, G.E. Karniadakis, Transport dissipative particle dynamics model for mesoscopic advection-diffusion-reaction problems, J. Chem. Phys. 143 (2015) 014101. https://doi.org/10.1063/1.4923254.

[69] N. Li, S. Chen, K. Xu, M.-T. He, M.-Q. Dong, Q.C. Zhang, N. Gao, Structural basis of membrane skeleton organization in red blood cells, Cell 186 (2023) 1912-1929.e18. https://doi.org/10.1016/j.cell.2023.03.017.

[70] D.S. Gokhin, V.M. Fowler, Feisty filaments: actin dynamics in the red blood cell membrane skeleton, Curr. Opin. Hematol. 23 (2016) 206–214. https://doi.org/10.1097/MOH.0000000000000227.

[71] N. Prasain, T. Stevens, The actin cytoskeleton in endothelial cell phenotypes, Microvasc. Res. 77 (2009) 53–63. https://doi.org/10.1016/j.mvr.2008.09.012.

[72] S. Mylvaganam, S.A. Freeman, S. Grinstein, The cytoskeleton in phagocytosis and macropinocytosis, Curr. Biol. 31 (2021) R619–R632. https://doi.org/10.1016/j.cub.2021.01.036.

[73] J.L. Rodríguez-Fernández, O. Criado-García, The Actin Cytoskeleton at the Immunological Synapse of Dendritic Cells, Front. Cell Dev. Biol. 9 (2021) 679500. https://doi.org/10.3389/fcell.2021.679500.

[74] P.-O. Persson, Mesh Generation for Implicit Geometries, 2004.

[75] P.-O. Persson, G. Strang, A Simple Mesh Generator in MATLAB, SIAM Rev. 46 (2004) 329–345. https://doi.org/10.1137/S0036144503429121.

[76] K. Kawauchi, H. Fujita, D. Miyoshi, E.K.F. Yim, H. Hirata, Cell and Molecular Mechanics in Health and Disease, BioMed Res. Int. 2017 (2017) 1–2. https://doi.org/10.1155/2017/2860241.

[77] S. Suresh, J. Spatz, J.P. Mills, A. Micoulet, M. Dao, C.T. Lim, M. Beil, T. Seufferlein, Connections between single-cell biomechanics and human disease states: gastrointestinal cancer and malaria, Acta Biomater. 1 (2005) 15–30. https://doi.org/10.1016/j.actbio.2004.09.001.

[78] C.T. Lim, E.H. Zhou, S.T. Quek, Mechanical models for living cells—a review, J. Biomech. 39 (2006) 195–216. https://doi.org/10.1016/j.jbiomech.2004.12.008.

[79] X. Li, Z. Peng, H. Lei, M. Dao, G.E. Karniadakis, Probing red blood cell mechanics, rheology and dynamics with a two-component multi-scale model, Philos. Trans. R. Soc. Math. Phys. Eng. Sci. 372 (2014) 20130389. https://doi.org/10.1098/rsta.2013.0389.

[80] H. Liu, Y. Sun, C.A. Simmons, Determination of local and global elastic moduli of valve interstitial cells cultured on soft substrates, J. Biomech. 46 (2013) 1967–1971. https://doi.org/10.1016/j.jbiomech.2013.05.001.

[81] D.A. Fedosov, B. Caswell, G.E. Karniadakis, Systematic coarse-graining of spectrin-level red blood cell models, Comput. Methods Appl. Mech. Eng. 199 (2010) 1937–1948. https://doi.org/10.1016/j.cma.2010.02.001.

[82] S. Eloul, E. Kätelhön, R.G. Compton, When does near-wall hindered diffusion influence mass transport towards targets?, Phys. Chem. Chem. Phys. 18 (2016) 26539–26549. https://doi.org/10.1039/C6CP05716K.

[83] M. González-Melchor, E. Mayoral, M.E. Velázquez, J. Alejandre, Electrostatic interactions in dissipative particle dynamics using the Ewald sums, J. Chem. Phys. 125 (2006) 224107. https://doi.org/10.1063/1.2400223.

[84] R.D. Groot, Electrostatic interactions in dissipative particle dynamics—simulation of polyelectrolytes and anionic surfactants, J. Chem. Phys. 118 (2003) 11265–11277. https://doi.org/10.1063/1.1574800.

[85] A. Gubbiotti, M. Chinappi, C.M. Casciola, EH-DPD: a dissipative particle dynamics approach to electrohydrodynamics, Eur. Phys. J. Plus 137 (2022) 572. https://doi.org/10.1140/epjp/s13360-022-02770-z.

[86] J. Smiatek, F. Schmid, Mesoscopic simulations of electroosmotic flow and electrophoresis in nanochannels, Comput. Phys. Commun. 182 (2011) 1941–1944. https://doi.org/10.1016/j.cpc.2010.11.021.

[87] C. Junghans, M. Praprotnik, K. Kremer, Transport properties controlled by a thermostat: An extended dissipative particle dynamics thermostat, Soft Matter 4 (2008) 156–161. https://doi.org/10.1039/B713568H.

Appendix

1. Script of Mesh Generation for Different Types of Cells

Presented herein is a script for the generation of surface meshes for three-dimensional geometric figures, employing Matlab syntax and constructed in accordance with the Distmesh toolkit. The Distmesh toolkit is accessible online. Notice that it has been observed in practical modeling endeavors that Distmesh exhibits reduced stability in mesh generation for three-dimensional shapes with excessive curvature, such as epithelial cells. These cells, characterized by a thickness markedly small relative to their length and width, lead to increased curvature at their edges.

```
% Define circular parameters: topological flag, and edge length
% leaf = 1; sphere = 2; capsule = 3; ellipsoid = 4; concave = 5
for flag = 1:5
    if flag == 1
        h0_values = [0.5,0.8,1,2,3];
    elseif flag == 2
        h0_values = [1,2,3,4,5];
    elseif flag == 3
        h0_values = [5,6,7,8.1,9];
    elseif flag == 4
        h0_values = [0.4,0.6,0.8,1,2];
    elseif flag == 5
        h0_values = [0.3,0.5,0.7,0.91,1.1];
    end

    for h0 = h0_values
        % Define the three-dimensional shape geometric parameters
        switch flag
            case 1
                % Rotation matrix rotating 60 degrees around the z-axis
                A = [1/2, -sqrt(3)/2, 0; sqrt(3)/2, 1/2, 0; 0, 0, 1];
                % Rotation matrix rotating 120 degrees around the z-axis
                B = [-1/2, -sqrt(3)/2, 0; sqrt(3)/2, -1/2, 0; 0, 0, 1];
                % The radii lengths of the flap ellipsoid along the x-axis, y-axis, and z-axis
```

```
            a = 48; b = 32; c = 8;
            % The radius length of the cellular ellipsoid
            d = 36; e = 36; f = c;
        case 2
            rs = 40; % radius of sphere
        case 3
            % Parameters of the hemisphere radius and cylinder height
            r = 50; h = 1900;
        case 4
            % The radii lengths of the flap ellipsoid along the x-axis, y-axis, and z-axis
            ea = 80; eb = 48; ec = 8;
        case 5
            D0 = 7.82; % cell diameter
            a0 = 0.0518; a1 = 2.0026; a2 = -4.491;
    end
    % Define SDF
    switch flag
        case 1
            fd = @(p) dunion(dunion(dunion(sum((p).^2./ ...
                repmat([a^2, b^2, c^2], size(p, 1), 1), 2) - 1, ...
                sum((p*A).^2./repmat([a^2, b^2, c^2], size(p, 1), 1), 2) - 1), ...
                sum((p*B).^2./repmat([a^2, b^2, c^2], size(p, 1), 1), 2) - 1), ...
                sum((p).^2./repmat([d^2, e^2, f^2], size(p, 1), 1), 2) - 1);
        case 2
            fd = @(p) dsphere(p,0,0,0,rs);
        case 3
            fd = @(p) p(:,1).^2 + p(:,2).^2 + (1/4) * (abs(p(:,3) - h/2) + ...
                abs(p(:,3) + h/2) - h).^2 - r^2;
        case 4
            fd = @(p) sum((p).^2./repmat([ea^2, eb^2, ec^2], size(p, 1), 1), 2) - 1;
        case 5
            fd = @(p)(D0 .* sqrt(1 - 4 .* (p(:,1).^2 + p(:,2).^2) / D0^2) .* ...
                (a0 + a1 .* (p(:,1).^2 + p(:,2).^2) / D0^2 + a2 .* (p(:,1).^2 + ...
                p(:,2).^2).^2 / D0^4)).^2 - p(:,3).^2;
    end
    % Define mesh generation parameters
    fh = @huniform; % uniform distribution
    % Define the size of the box
    switch flag
        case 1
            box0 = [-(max(a,b)+1),-(max(a,b)+1),-(c+1); ...
                (max(a,b)+1),(max(a,b)+1),(c+1)];
```

```
            case 2
                box0 = [-rs,-rs,-rs; rs,rs,rs];
            case 3
                box0 = [-r,-r,-(2*r+h); r,r,(2*r+h)];
            case 4
                box0 = [-2*ea,-2*eb,-2*ec; 2*ea,2*eb,2*ec];
            case 5
                box0 = [-D0,-D0,-D0; D0,D0,D0];
        end
        box = 1.1*box0;
        [p,t] = distmeshsurface(fd,fh,h0,box); % Mesh generation
    end
end
```

2. Mesh Results of Different Types of Cells

In the evaluation of mesh generation quality for computational simulations, two standard metrics are commonly employed: the minimum mesh quality which is the minimized value of $(2 \times \sqrt{3} \times \text{area} \div \text{perimeter})$ for all every triangular area, and the coefficient of variation of area which is defined as the ratio of the standard deviation to the mean for all triangular area. When the minimum mesh quality approaches zero, it typically indicates that the elements within the mesh are highly anisotropic, exhibiting a slender or elongated shape. A lower value of coefficient of variation of area signifies a more uniform distribution of element areas with the mesh, which is generally indicative of superior mesh quality. Figure 26-30 evaluates different shapes cellular mesh results.

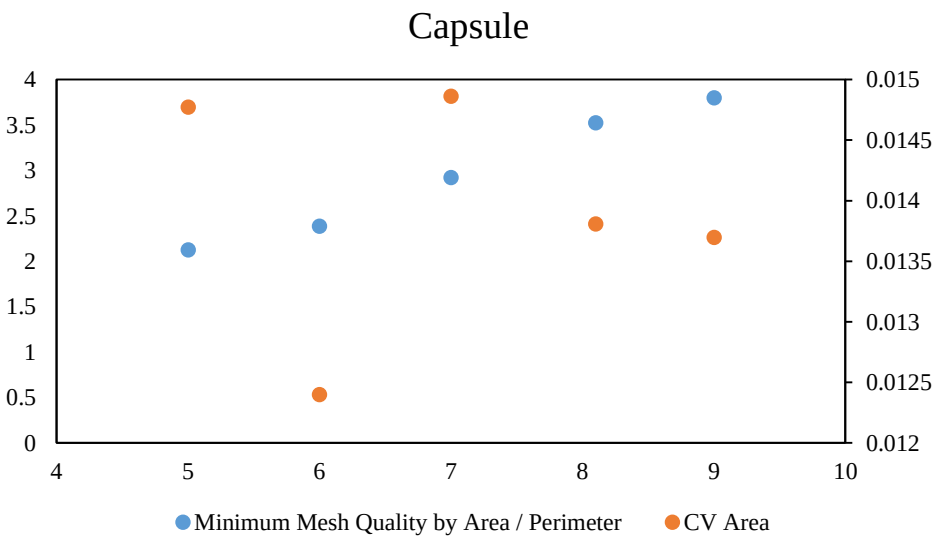

Figure 26 Evaluation of Capsule Shape Mesh Result

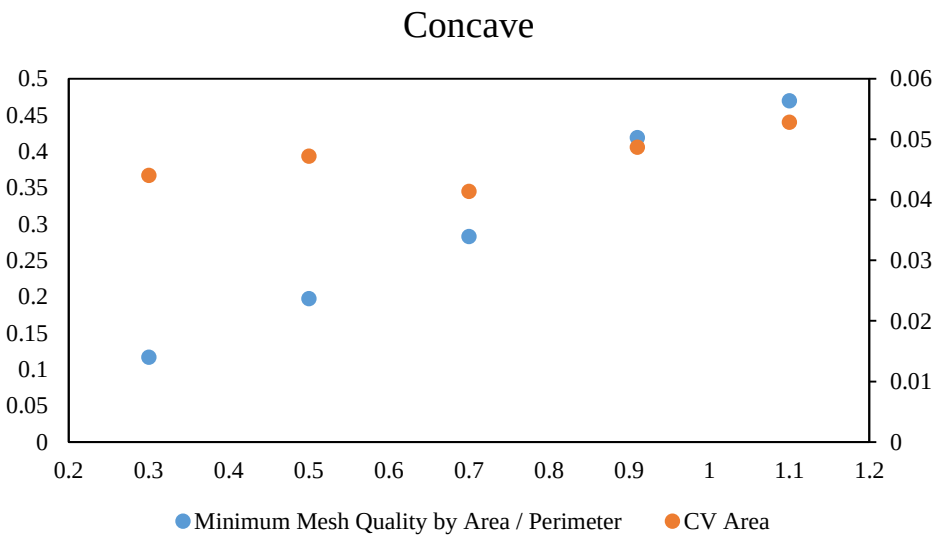

Figure 27 Evaluation of Concave Shape Mesh Result

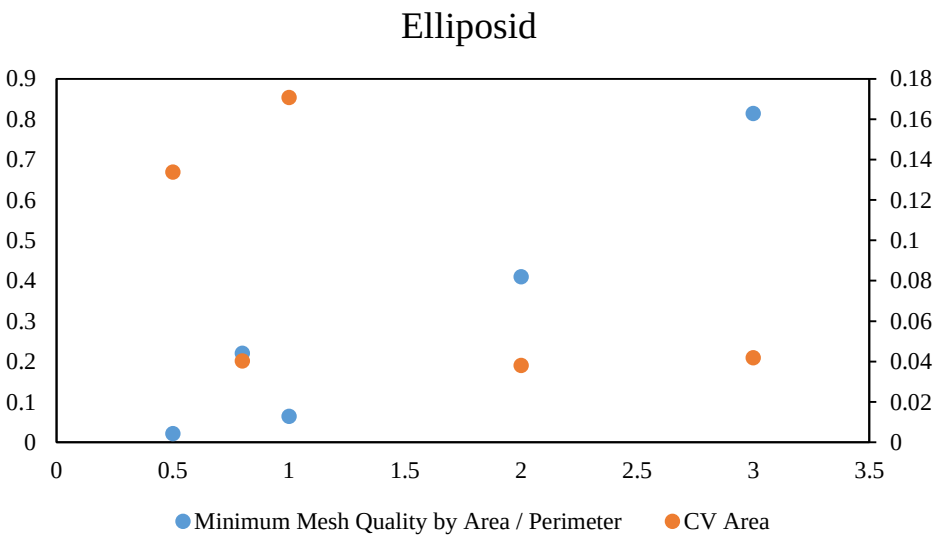

Figure 28 Evaluation of Ellipsoid Shape Mesh Result

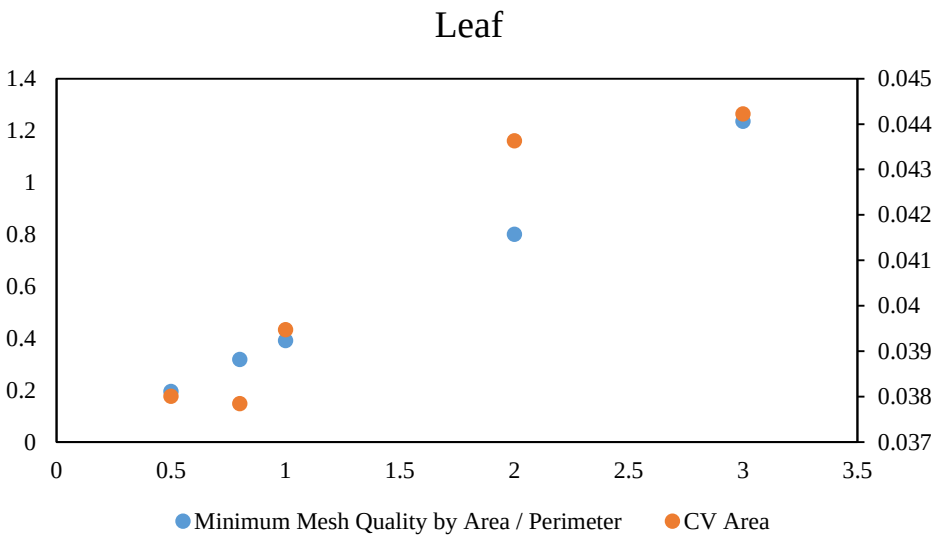

Figure 29 Evaluation of Leaf Shape Mesh Result

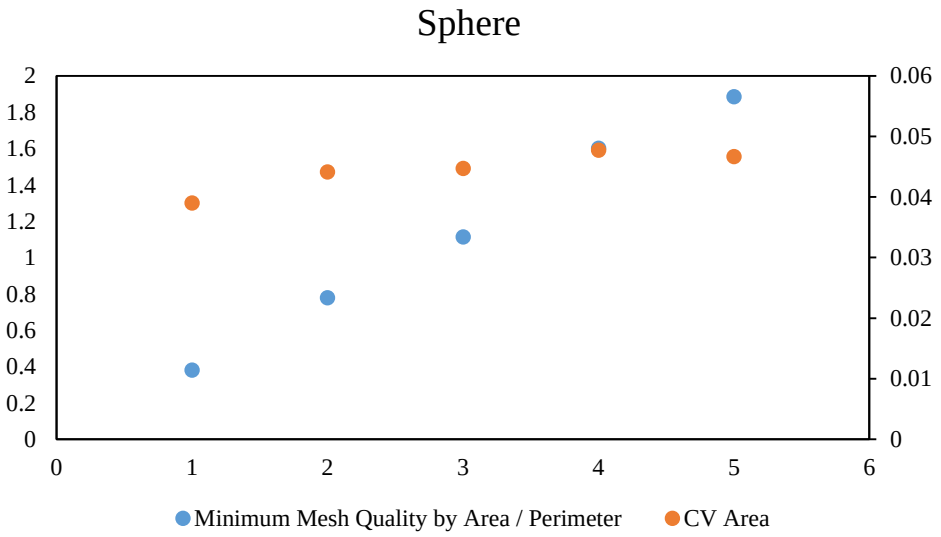

Figure 30 Evaluation of Sphere Shape Mesh Result

Table 8 Percent of vertices with different connections for capsule shape

length of edge	Percentage of vertices with 5 connections	Percentage of vertices with 6 connections	Percentage of vertices with 7 connections	Percentage of vertices with other connections
5	0.28%	99.47%	0.24%	-
6	0.50%	99.05%	0.45%	-

7	0.41%	99.24%	0.34%	-
8.1	0.47%	99.16%	0.37%	-
9	0.45%	99.23%	0.32%	-

Furthermore, because the structural characteristics of the cell membrane's cytoskeleton, specific requirements are imposed on the connectivity of grid nodes. A grid with 6-connectivity is considered the most ideal configuration in this context. Consequently, further analysis has been conducted to examine the proportion of nodes with different connectivity patterns across cells of various shapes. Table 9-12 amylases these features.

Table 9 Percent of vertices with different connections for concave shape

length of edge	Percentage of vertices with 5 connections	Percentage of vertices with 6 connections	Percentage of vertices with 7 connections	Percentage of vertices with other connections
0.3	7.39%	85.81%	6.80%	-
0.5	9.38%	82.84%	7.77%	-
0.7	9.31%	84.31%	6.37%	-
0.91	12.21%	80.23%	6.40%	1.16%
1.1	13.70%	78.77%	5.48%	2.05%

Table 10 Percent of vertices with different connections for ellipsoid shape

length of edge	Percentage of vertices with 5 connections	Percentage of vertices with 6 connections	Percentage of vertices with 7 connections	Percentage of vertices with other connections
0.4	3.91%	92.19%	3.88%	0.02%
0.6	4.13%	91.76%	4.11%	0.01%
0.8	4.16%	91.74%	4.06%	0.02%
1	4.58%	90.88%	4.53%	0.01%
2	5.90%	88.36%	5.74%	-

Table 11 Percent of vertices with different connections for leaf shape

length of edge	Percentage of vertices with 5 connections	Percentage of vertices with 6 connections	Percentage of vertices with 7 connections	Percentage of vertices with other connections
0.5	3.83%	92.36%	3.81%	0.00%
0.8	4.62%	90.81%	4.57%	-
1	5.10%	89.87%	5.03%	-
2	6.93%	86.41%	6.66%	-
3	7.26%	86.09%	6.65%	-

Table 12 Percent of vertices with different connections for sphere shape

length of edge	Percentage of vertices with 5 connections	Percentage of vertices with 6 connections	Percentage of vertices with 7 connections	Percentage of vertices with other connections
1	4.99%	90.05%	4.95%	-
2	6.39%	87.38%	6.23%	-
3	7.50%	85.35%	7.14%	-
4	10.91%	78.85%	10.24%	-
5	9.70%	81.59%	8.71%	-

Acknowledgements

I hereby extend my profound appreciation to all individuals who have offered their unwavering support and assistance throughout my academic journey spanning over two decades.

Foremost, my heartfelt thanks are directed to my mentors, Prof. Reiji Noda and Prof. Wei Ge. Their belief in my potential opened the gateway to my doctoral pursuit. Under their meticulous guidance and profound expertise, I have experienced significant enhancement in my scholarly capabilities and intellectual acumen. Their insightful feedback and critical thinking have consistently illuminated the core issues of my research, enabling me to refine my focus, address gaps, and steadily advance my work in the right direction.

I am equally grateful to Prof. Wei Chen, whose invaluable suggestions on the technical aspects of my research were instrumental in overcoming numerous challenges, thereby facilitating the successful completion of my projects. Prof. Yufei Xia also deserves special mention for his enlightening discussions that greatly aided my understanding of the biological context of my study.

My gratitude extends to the members of the review committee for their meticulous evaluation of my dissertation. Their constructive criticisms and valuable suggestions not only highlighted areas for improvement but also deepened my understanding of the field.

A special word of thanks goes to my family and friends, whose encouragement and comfort during moments of exhaustion and uncertainty were invaluable. Their support provided the space I needed to focus more intensely on my research endeavors.

I also wish to express my sincere appreciation to Ms. Mayumi Tanaka, secretary to Prof. Reiji Noda. During my tenure at Gunma University, her assistance in navigating complex administrative tasks and providing crucial information was indispensable. Her support during my illness, especially in a foreign land with language barriers, in resolving communication and transportation issues, was extraordinary. Her kindness and gentleness will always be remembered with gratitude.

Furthermore, my thanks to Mr. Teng Ma, Ms. Cui Liu, Ms. Yanfeng Shi, and Ms. Jian Wang from the Institute of Process Engineering, Chinese Academy of Sciences, for their consistent support in both academic and personal matters, ranging from coordinating meetings with professors to assisting in life arrangements.

Lastly, I acknowledge all those who have supported and encouraged me, whose names I may not have listed, but whose contributions are no less significant. Your dedication and silent concern have been pivotal in my journey. Your interest and support in my studies and research have been crucial in propelling me forward towards excellence.

As I conclude this acknowledgment in my doctoral thesis, I fondly recall the care and assistance I received during my doctoral studies. Without your support and encouragement, my academic path would have been less smooth. Once again, I extend my deepest gratitude and respect to each one of you for enabling my growth and improvement on this academic path.

Publication and Conference

Journal publications

X.W. Liu, W. Chen, Y.F. Xia, G.H. Ma, R.J. Noda, W. Ge, Pickering emulsion transport in skeletal muscle tissue: A dissipative particle dynamics simulation approach, Chin. J. Chem. Eng. 2024. https://doi.org/10.1016/j.cjche.2024.01.002